UC Irvine
UC Irvine Previously Published Works

Title

Glioma-Induced Alterations in Neuronal Activity and Neurovascular Coupling during Disease Progression

Permalink

https://escholarship.org/uc/item/2g52w7r4

Journal

Cell Reports, 31(2)

ISSN

2639-1856

Authors

Montgomery, Mary Katherine

Kim, Sharon H

Dovas, Athanassios

et al.

Publication Date

2020-04-01

DOI

10.1016/j.celrep.2020.03.064

Copyright Information

Peer reviewed

Glioma-Induced Alterations in Neuronal Activity and Neurovascular Coupling during Disease Progression

Mary Katherine Montgomery[1,6], **Sharon H. Kim**[1,6], **Athanassios Dovas**[2,6], **Hanzhi T. Zhao**[1], **Alexander R. Goldberg**[2], **Weihao Xu**[1], **Alexis J. Yagielski**[1], **Morgan K. Cambareri**[1], **Kripa B. Patel**[1], **Angeliki Mela**[2], **Nelson Humala**[2], **David N. Thibodeaux**[1], **Mohammed A. Shaik**[1], **Ying Ma**[1], **Jack Grinband**[3], **Daniel S. Chow**[4], **Catherine Schevon**[5], **Peter Canoll**[2,7,*], **Elizabeth M.C. Hillman**[1,*]

[1]Laboratory for Functional Optical Imaging, Zuckerman Mind Brain Behavior Institute, Departments of Biomedical Engineering and Radiology, Columbia University, New York, NY 10027, USA

[2]Department of Pathology and Cell Biology, Irving Cancer Research Center, Columbia University Irving Medical Center, New York, NY 10032, USA

[3]Department of Psychiatry, New York State Psychiatric Institute, Columbia University Irving Medical Center, New York, NY 10032, USA

[4]Department of Radiological Sciences, University of California, Irvine, Orange, CA 92868, USA

[5]Department of Neurology, Columbia University Irving Medical Center, New York, NY 10032, USA

[6]These authors contributed equally

[7]Lead Contact

SUMMARY

Diffusely infiltrating gliomas are known to cause alterations in cortical function, vascular disruption, and seizures. These neurological complications present major clinical challenges, yet their underlying mechanisms and causal relationships to disease progression are poorly characterized. Here, we follow glioma progression in awake Thy1-GCaMP6f mice using *in vivo* wide-field optical mapping to monitor alterations in both neuronal activity and functional hemodynamics. The bilateral synchrony of spontaneous neuronal activity gradually decreases in glioma-infiltrated cortical regions, while neurovascular coupling becomes progressively disrupted

*Correspondence: pc561@cumc.columbia.edu (P.C.), elizabeth.hillman@columbia.edu (E.M.C.H.).

compared to uninvolved cortex. Over time, mice develop diverse patterns of high amplitude discharges and eventually generalized seizures that appear to originate at the tumors' infiltrative margins. Interictal and seizure events exhibit positive neurovascular coupling in uninfiltrated cortex; however, glioma-infiltrated regions exhibit disrupted hemodynamic responses driving seizure-evoked hypoxia. These results reveal a landscape of complex physiological interactions occurring during glioma progression and present new opportunities for exploring novel biomarkers and therapeutic targets.

In Brief

The glioma microenvironment involves multiple cell types. Montgomery et al. utilize *in vivo* wide-field cortical imaging in awake mice to characterize both neuronal activity and hemodynamics during glioma progression. Observed tumor-localized alterations in neuronal synchrony and neurovascular coupling, interictal events, and seizures reveal potential functional contributions to glioma progression.

Graphical Abstract
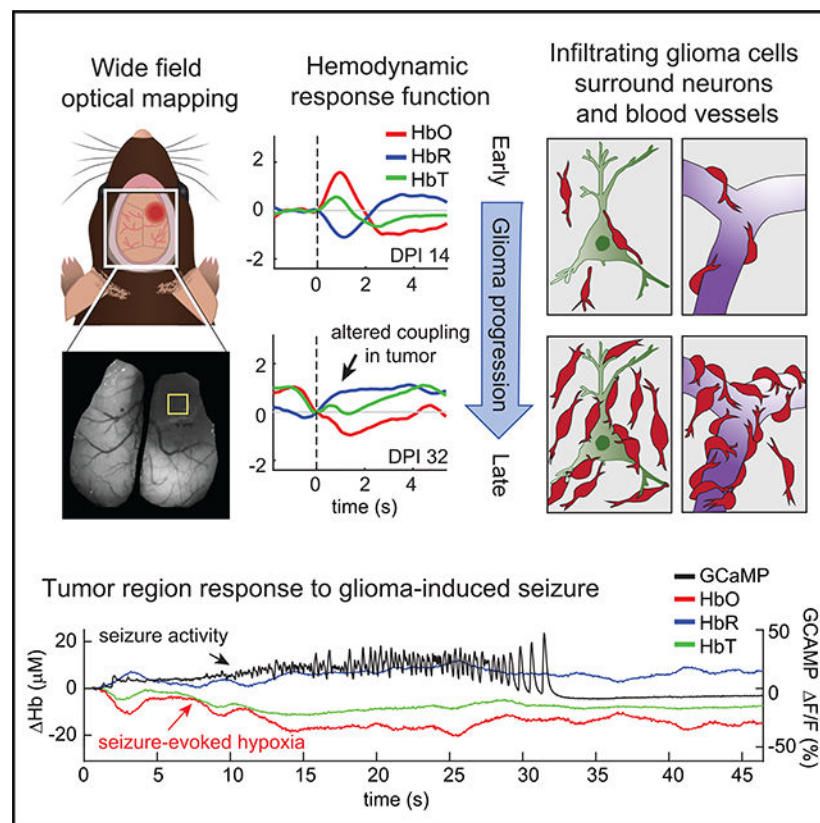
INTRODUCTION

Gliomas are primary brain neoplasms characterized by diffuse infiltration of glioma cells into surrounding brain tissue, where they interact with neurons, astrocytes, and blood vessels (Cuddapah et al., 2014; Torres and Canoll, 2019). Glioma patients often present with

neurological symptoms that result from functional alterations in the infiltrated cortex. Seizures, the most common neurological symptom, afflict >80% of low-grade glioma patients and 50%–60% of high-grade glioma patients and can contribute significantly to the deterioration of cognitive function (Klein et al., 2003; Rudà et al., 2010).

The clinical management of glioma-associated seizures is confounded by complex interactions between therapies targeting tumor progression, anti-epileptic drugs, and tumor pathophysiology itself (de Groot et al., 2012; van Breemen et al., 2007). Currently, the most effective therapeutic approach to ameliorating seizures in glioma patients is maximizing tumor resection to include the infiltrating tumor margins (Pallud et al., 2014). However, when glioma patients fail therapy and their tumors recur, they often present with new or worsening seizures (Smits and Duffau, 2011). These clinical observations suggest that glioma-induced epileptogenesis is a dynamic process caused by the infiltration of glioma cells into the cortex, which leads to progressive alterations in focal cortical activity.

Several studies have demonstrated that infiltrating glioma cells can induce neuronal hyperexcitability and seizures through several mechanisms, including aberrant release of the excitatory neurotransmitter glutamate, and loss of γ-aminobutyric acid (GABA)ergic inhibitory signals (Buckingham et al., 2011; Campbell et al., 2012, 2015). Recent studies have also shown that neuronal activity and hyperexcitability can stimulate glioma cell proliferation, suggesting that glioma-induced seizures may contribute to increased tumor growth and progression (Robert et al., 2015; Vecht et al., 2014; Venkataramani et al., 2019; Venkatesh et al., 2015, 2019, 2017). This complex interplay between glioma progression and aberrant neural activity remains poorly understood, and yet underlies many aspects of tumor progression, directly affecting the clinical course of almost all low-grade glioma patients.

Patients with seizures also develop brief interictal epileptiform discharges that do not cause overt behavioral manifestations, but can occur much more frequently than observable seizures (Selvitelli et al., 2010). However, the causes and cognitive effects of these smaller interictal events (IIEs) remain controversial (Avanzini et al., 2013; Faught et al., 2018), and their relationship to tumor progression is not well characterized.

Glioma cells have also been observed to interact closely with blood vessels, migrating along them as conduits during tumor spread, and disrupting their structural and functional integrity (Farin et al., 2006; Watkins et al., 2014). These vascular interactions prompt the question of whether tumors could impact the coupling between neuronal activity and vascular dynamics during glioma-infiltration. Such neurovascular interactions could contribute to the disturbed functional and metabolic state of the brain during tumor progression, particularly in the context of abnormal neural events such as IIEs and seizures. Although not studied in the setting of gliomas, epileptic seizures have been shown to have profound hemodynamic effects (Ma et al., 2013; Schwartz, 2007; Zhao et al., 2009).

Glioma-related changes in neurovascular coupling could also affect the blood-oxygen-level-dependent (BOLD) signals measured using functional magnetic resonance imaging (fMRI). Understanding these effects is especially important since one of the only clinical uses of fMRI is pre-surgical planning for tumor resections, seeking to identify the location of key

functional brain regions to be preserved or removed (Genetti et al., 2013; Petrella et al., 2006). Tumor-dependent alterations in neurovascular coupling could lead to misinterpretation of fMRI data, and errors in the localization of functional boundaries. Several recent human resting-state fMRI studies have also shown that gliomas can cause focal changes in the BOLD signals detected in the tumor and surrounding infiltrated cortex, characterized by a loss of synchrony between the tumor and the contralateral hemisphere (Agarwal et al., 2016; Bowden et al., 2018; Chow et al., 2016). Although these studies could not disambiguate whether changes in BOLD were caused by altered neuronal activity, neurovascular coupling, or both, they suggest that vascular signals could be helpful biomarkers of tumor progression.

To understand these diverse, dynamic physiological interactions between tumor progression, neuronal activity, and hemodynamics, we need to monitor the *in vivo* functioning brain and assess the alterations of both neuronal activity and neurovascular responses during glioma progression. Here, we combined novel methods for *in vivo,* longitudinal wide-field optical mapping (WFOM) in awake-behaving Thy1-GCaMP6f mice (Ma et al., 2016a) with an orthotopic model of glioma, characterized by diffuse infiltration of the cerebral cortex with perivascular patterns of invasion, and intermingling of tumor cells with neurons. Neuronal activity and hemoglobin oxygenation dynamics were simultaneously imaged across both hemispheres of the dorsal cortex throughout the course of disease progression within individual mice.

This imaging approach enabled direct observations of longitudinal changes in the properties of spontaneous and evoked neuronal events across the cortex including intracortical desynchronization, progressively worsening IIEs, and eventually spontaneous seizures. These data also afforded the ability to explore the way in which these different neuronal events were coupled to changes in hemodynamics as a function of disease progression. Our analysis revealed significant neurovascular disruption within tumor-burdened regions, a finding that has important implications for interpretation of fMRI data acquired for resection guidance, while also suggesting ways in which altered coupling could contribute to exacerbation of tumor-related damage and even hasten tumor progression.

These results provide new insights into the progressive interplay between glioma invasion and cortical function, while demonstrating that WFOM is a valuable tool for characterizing disease and potentially screening for new therapeutic targets to reduce the morbidity and mortality of glioma. These findings add to the growing body of evidence suggesting a bidirectional relationship between alterations in cortical activity and glioma growth and progression (Buckingham et al., 2011; Campbell et al., 2012; Gillespie and Monje, 2018; John Lin et al., 2017; Johung and Monje, 2017; Tewari et al., 2018; Venkatesh et al., 2017).

RESULTS

WFOM was used to longitudinally image GCaMP6f fluorescence and hemodynamics across the cortex of adult Thy1-GCaMP6f mice following intracerebral injection of PDGFA$^+$/TP53$^{-/-}$ mouse glioma cells into the subcortical white matter of right frontal cortex. Thy1-GCaMP6f mice express a calcium-sensitive green fluorescent protein in their excitatory

neurons of layers 2/3 and 5, and thus changes in cortical fluorescence reveal changes in neuronal intracellular calcium levels. A large, bilateral thinned-skull cranial window was formed at the same time as tumor initiation, and after recovery, the mice were imaged during sessions lasting up to 2 hr in which they were head-restrained but awake, starting at 4 days post injection (DPI) and continuing until 36 DPI. WFOM images were acquired using a camera focused onto the cranial window with a sequence of light emitting diodes (LEDs) illuminating to record green fluorescence from GCaMP6f under blue illumination, and then green and red reflectance to enable calculation of changes in the concentration of oxyhemoglobin (HbO), deoxyhemoglobin (HbR), and total hemoglobin (HbT = HbO + HbR) as detailed in STAR Methods. Reflectance measurements were also used to correct GCaMP6f fluorescence measurements for the effects of changes in hemoglobin absorption (Ma et al., 2016a). All animals expired at the end of the study and their brains were extracted for histological processing. Additional Thy1-GCaMP6f mice were implanted with tumors in the same way to permit *in vivo* two-photon investigations as well as more comprehensive histological analysis at interim time-points, while sham animals receiving intracortical injections of saline were also imaged longitudinally as controls.

Diffuse Infiltration of Glioma into the Cortex of Thy1-GCaMP6f Mice Leads to Progressive Alterations in Neurons and Blood Vessels

Histological analysis demonstrated that gliomas produced using this method showed a progressive and diffuse infiltration into the cortex, recapitulating the patterns of infiltration seen in human gliomas (Figure 1A). Perineuronal satellitosis was prominent, particularly at the infiltrative margins of the tumor (Figure 1B). The density of neurons was significantly decreased in the highly cellular core of the tumors, and to a lesser extent at the infiltrative margins (Figures S1A and S1B). Infiltrating glioma cells also accumulated near blood vessels (stained using the isolectin IB4; Figure 1C).

Notably, immunofluorescence analysis for the water channel aquaporin 4 (AQP4), which in healthy brain tissue is discretely localized in astrocyte endfeet-contacting vessels (Gleiser et al., 2016; Mader and Brimberg, 2019; Nagelhus et al., 2004; Nielsen et al., 1997), revealed that astrocyte endfeet remained closely associated with vessels at the infiltrative margins (Figure 1D). In contrast, in the highly cellular core of the tumor, AQP4 staining was diffusely distributed on the GFAP+ processes of reactive astrocytes (Figures 1D and S1E). This finding is consistent with previous studies showing that the perivascular distribution of AQP4 is disrupted in reactive astrocytes in a variety of neuropathological conditions (Liu et al., 2015; Wanner et al., 2013). We also examined specific changes in the vasculature of the glioma-infiltrated cortex using CD34, a glycoprotein present on vascular endothelial cells (Nielsen and McNagny, 2008). Confocal images acquired in the highly cellular core of the tumor showed that vessels had an abnormal morphology and were encased by glioma cells (Figure 1C). We also noted that the levels of CD34 immunoreactivity in the vasculature within the tumor core was significantly increased compared to uninvolved, contralateral cortex, and there was a significant increase in the overall density of CD34+ vessels within the tumor core by 28 DPI (Figure 1E). Similar changes in AQP4 and CD34 are seen in surgical samples of human gliomas (Clara et al., 2014; Noell et al., 2012; Smith and

Verkman, 2015), and their expression is regulated by HIF-1α, potentially reflecting reactive responses to local tissue hypoxia (Nigim et al., 2015) (Mou et al., 2010).

Post-mortem analysis of the infiltrating margins of tumors from the mice that underwent *in vivo* imaging allowed us to interrogate the patterns of glioma infiltration through layers 2/3 and 5. In these mice, glioma cells intermingled with GCaMP6f^{+} neurons (Figure S1C; Video S1), and appeared to migrate along the abluminal surface of blood vessels in close association with AQP4+ astrocyte endfeet (Figure S1D). These findings reveal progressive disruption of neuronal and vascular organization in the glioma-bearing cortex, which is most severe in the highly cellular tumor core, but remains relatively intact at the infiltrated margins of the tumor.

Gradual Loss of GCaMP Fluorescence Reflects Loss of Neurons within the Tumor

Figure 2 shows a sequence of longitudinal *in vivo* WFOM recordings in one animal during the progression of tumor growth in the anterior right side of the cortex. The raw GCaMP6f fluorescence images show a gradually expanding dark area around the tumor cell injection site in the right anterior quadrant. Corresponding green light reflectance images do not show the same darkening, confirming that this effect corresponds to decreasing GCaMP6f fluorescence and not increasing absorption, for example from increased vascular density (Figure 2A).

This gradual GCaMP6f signal decrease is consistent with the progressive loss of neurons, which is most pronounced in the highly cellular core of the tumor (as shown in Figures 1D and S1B). To confirm this effect, we acquired *in vivo* two-photon microscopy data in an awake mouse implanted with chronic glass windows placed both over the tumor injection site and the equivalent region of the contralateral cortex (Figure S2). While spontaneous firing of individual neurons was seen on both the tumor and contralateral sides, fewer neuronal cell bodies and fewer overall events were detected on the glioma side during every imaging session. *Ex vivo* imaging of an acute brain slice from the same mouse, as well as *ex vivo* histology, confirmed decreased density of neuronal soma on the tumor side, as well as decreased overall GCaMP6f signal owing to the increasing density of glioma cells infiltrating the neuropil (Figures S2A, S2B, S2E, and S2F).

Resting State Neuronal and Hemodynamic Activity Becomes Less Bilaterally Correlated in Tumor Regions during Glioma Progression

Longitudinal WFOM data in Figure 2C shows example time series of neural activity and hemodynamics from the tumor and the contralateral anterior region during tumor progression. At early time points, neuronal activity on both sides of the cortex is clearly correlated, and the same is true for bilateral cortical hemodynamics. However, as the tumor progresses, neuronal activity in the tumor region can be seen to decrease both in terms of its % amplitude, and its high frequency content compared to the contralateral region (gray and black traces). Hemodynamic activity in the tumor region also shows a progressive attenuation of fluctuations, particularly in HbT. This effect can also be seen in the representative real-time WFOM data movie (Video S2).

To assess how these activity changes affect interregional synchrony, pixel-by-pixel Pearson's correlation analysis was performed. The maps shown in Figure 2B depict the correlation of signals relative to the anterior left frontal seed region (contralateral to the tumor) for both GCaMP6f and HbT. These correlation maps show a gradual decrease in regional correlation of both neuronal and hemodynamic signals at the core of the tumor as it progresses, with more significant changes visible in the HbT correlation maps, a pattern that was consistent across all animals (Figure S3). Notably, the region corresponding to the margin of the tumor shows a higher HbT correlation with the contralateral cortex than the tumor core, even though both regions show neuronal loss, evident from the low GCaMP signal (Figures 2A and 2B). These findings suggest that the infiltrating margin of the tumor is functionally distinct from the tumor core, particularly with regard to hemodynamic activity.

To quantify these trends, bilateral correlations among 4 brain regions were compared: the anterior right frontal cortex (tumor region), the anterior left frontal cortex (contralateral to the tumor region), and visual cortex areas ipsilateral and contralateral to the tumor (Figure 2D). While almost no changes in bilateral correlation were seen for posterior, non-tumor-bearing visual cortex regions, significant and systematic decreases in bilateral correlation were seen for the frontal regions as the tumor progressed unilaterally. The difference in the slope of this correlation trend between tumor and non-tumor regions was significant, and more pronounced for hemodynamics than for GCaMP6f signals (Figure 2D), although we note that GCaMP6f analysis may also be impacted by the gradual decrease in signal to noise caused by the significant loss of GCaMP fluorescence in the tumor as it progresses. A consistent effect was seen in all 3 animals (Figure S3). As shown in Figure S4, sham saline-injected animals retained bilateral correlations over similar time-spans of analysis, confirming that loss of correlation was due to the growth of the tumor and not due to injection-associated reactive astrogliosis, which remained localized at the injection site.

The significance of these decorrelations relates to the field of resting state fMRI. The BOLD signals detected in resting state fMRI correspond to fluctuations in [HbR], which are correlated within brain-wide functional connectivity networks (Raichle et al., 2001). Recent studies have demonstrated that brain-wide patterns of neuronal activity are predictive of hemodynamic fluctuations, suggesting that resting-state functional connectivity depicts an important property of brain-wide neuronal dynamics (Ma et al., 2016b). Our results demonstrate that glioma infiltration disrupts the otherwise strong bilateral synchrony of both resting-state neuronal and hemodynamic fluctuations, a feature consistent with a recent study that noted the ability of resting-state fMRI analysis to delineate glioma tumor margins (Chow et al., 2016).

Glioma Causes Focal Disruption of Stimulus-Evoked Neurovascular Responses

Our resting state analysis demonstrated that tumor growth disrupts the synchrony of both spontaneous neuronal activity and hemodynamics in the awake brain (Ma et al., 2016b), but did not directly assess the coupling relationship between neuronal activity and hemodynamics. It is well described that in the normal brain, stimulus-evoked neuronal activity generates a stereotyped increase in local blood flow, driving an increase in HbT and HbO and a decrease in HbR. The positive BOLD response to a stimulus detected in fMRI

corresponds to this decrease in [HbR], providing a surrogate measure of neural activity (Hillman, 2014; Kwong et al., 1992).

To explore the effect of glioma progression on the neurovascular response to external stimulation, in every WFOM imaging session, mice underwent a sequence of 60 trials in which they received 5-s tactile whisker stimulations to either their right or left whisker pad at 30-s intervals. Trials in which significant other activity such as running occurred during stimulus delivery were excluded from further analysis.

Figures 3A–3C show whisker stimulus results for mouse 2 from DPI 11 to 32, while Figure S5 shows response maps and time-courses for all 3 mice to both left and right whisker stimuli at early and late time-points. In all mice, the tumor did not extend into the whisker region of the cortex. Accordingly, although the spatial and temporal responses to stimulus within the whisker barrel are variable, no systematic disease-related distortions of the response are evident. This result shows that despite significant progression of the tumor, neural circuitry and brain physiology was maintained in surrounding cortex.

However, examining signals within other regions of interest (ROIs) across the cortex, we note that tactile whisker stimulus in the awake mouse also evokes a smaller, cortex-wide neural response. Although this neural response is less well characterized, it is accompanied by a stereotypical hemodynamic response (Figure 3B). It is thus possible to evaluate the coupling relationship between these observed neuronal and hemodynamic responses within and around the tumor using deconvolution (Ma et al., 2016b) to estimate each region's hemodynamic response function (HRF), as shown in Figure 3C. These deconvolved hemodynamic response functions depict consistent patterns of normal functional hyperemia throughout uninfiltrated regions of the cortex at both early and late time-points. However, extracted HRFs were progressively attenuated and distorted within the glioma-infiltrated regions. A similar progression is shown for mouse 3 in Figure S6, with additional examples in Figure S5 across all mice.

A summary metric was compared across all animals, calculated as the integral of the HRF during the first 1.8 s of the response. Plotted in Figure 3D, progressively disrupted neurovascular coupling within the tumor region can be seen in all mice, with a trend toward higher [HbR] and lower [HbO] following stimulation compared to unaffected regions. This pattern is consistent with impaired coupling and net deoxygenation of the tumor-burdened cortex, suggesting a mismatch between the delivery of fresh, oxygenated blood, and consumption of oxygen within the tumor.

Interictal Events Accompany Tumor Progression and Evoke Altered Neurovascular Coupling in Regions of Tumor Infiltration

Over the 35 days of longitudinal imaging, the glioma-bearing mice developed increasingly abnormal neuronal activity, in particular, spontaneous high amplitude discharges seen as sharp, high amplitude increases in GCaMP6f fluorescence with associated hemodynamic changes. We interpret these patterns to be tumor-related interictal events (IIEs) (Figures 4B and 4C; Video S3). Events sometimes occurred in quick successive trains, while some occurred individually. Some events extended across all regions of the cortex, while others

appeared to remain more local (Figures 4B and 4C). Spatially dependent onset time analysis of successive IIE events within a single trial at DPI 35 shows widely varying initial locations, patterns, and speed of spread, although involvement of the tumor margin is clear in many cases (Figure 4D). The occurrence of these events across all mice and imaging sessions is depicted in detail in Figure S7 and summarized in Figure 4E. The overall frequency of IIEs correlated with the gradual growth of the tumor (with IIEs starting after 14 DPI). These events are not seen in WFOM recordings of healthy Thy1-GCaMP6f mice (Ma et al., 2016b).

The presence of spontaneous IIEs afforded the opportunity to assess how vascular responses are coupled to IIEs, both in tumor-burdened regions and the rest of the cortex. Analysis was performed using spike-triggered averaging centered on the GCaMP peak of identified IIEs and results are shown for tumor-infiltrated versus distant cortex in Figures 5 and S8. In regions distant from the tumor, hemodynamic coupling to IIEs was found to be positive, corresponding to an increase in perfusion leading to increased HbT and HbO and a decrease in HbR, similarly to a "positive BOLD" hemodynamic response to stimulus (compare to Figure 3). However, in glioma-infiltrated cortex, the same IIEs were associated with a very different hemodynamic response whose peak is significantly delayed and attenuated compared to healthy cortex, and includes a small inverted hemodynamic response that begins before the peak of the IIE. These patterns were consistent across individual events, in individual animals and between animals (Figures 5B–5D; Figures S8B–S8D). These delays and reduced positive amplitude of hemodynamic responses to IIEs in tumor regions (relative to the amplitude of local GCaMP6f signals) suggest that this neurovascular impairment is likely under-serving the metabolic needs of the tumor region during these high amplitude spontaneous neuronal events.

Spontaneous Seizures in Glioma-Bearing Mice Reveal Differences in the Neurovascular Response in Tumor versus Distant Cortical Regions

In addition to IIEs, our WFOM imaging sessions captured several spontaneous generalized seizure events in the late stage of tumor progression in two of the mice, as shown in Figures 6, 7, and S9, and Videos S4 and S5. Our real-time recordings of the cortical representations of these spontaneous seizure events permitted observation of the progression and spread of high amplitude neuronal activity, as well as concomitant hemodynamic responses to this seizure activity. In all seizures observed, the event began as a series of high amplitude spikes consistent with IIE characteristics, with highest signal intensities initially seen at the infiltrative margins of the tumor. This high intensity neuronal activity can then be seen to spread to the surrounding cortex in both hemispheres (Figure 6C).

Neuronal and hemodynamic signals extracted from the tumor and contralateral cortex are plotted in Figure 6, while Figures 7A and 7B, shows signals as a function of distance from the tumor center from anterior to posterior cortex for the seizure shown in Figure 6 and Video S4. Examining hemodynamics associated with seizure activity in non-tumor-bearing cortex reveals a clear positive coupling to initial IIEs, with large increases in HbT and HbO and decreases in HbR, as is also observed for both stimulus-evoked neuronal activity (Figure 3) and non-seizure-initiating IIEs (Figure 5). However, as neuronal events become more

rapid and then further intensify, we note that the hemodynamic response does not exhibit a proportional increase.

To test the linearity of the vascular response to the seizure, a canonical HRF was derived by averaging the HbT response from the four IIEs that occurred at the start of the seizure. This response was then convolved with the GCaMP6f fluorescence signal for the whole seizure. As shown in Figure 7C(i), in cortex contralateral to the tumor, a linear hemodynamic response would predict an almost 10-times higher peak HbT response than observed. We infer that the maximum amplitude of the hemodynamic response to seizure activity in non-tumor-bearing cortex is limited by the maximal possible dilation of cortical vessels. The gradual decrease in HbO and increase in HbR seen during this "HbT saturation" state is consistent with oxygen consumption outstripping oxygen delivery, suggesting that widespread tissue hypoxia occurs during seizures.

Examining hemodynamics within the tumor-burdened region for the same seizure event (Figure 6), we see an altered, attenuated, and delayed hemodynamic response to the initial IIEs, consistent with IIE results shown in Figure 5, but with an even more pronounced post-event undershoot in HbT. Using the same analysis method as above, convolution of this altered HRF with neuronal activity in the tumor region during the seizure actually predicts a negative HbT response (hypoperfusion) to the seizure activity that quite closely matches measured HbT, without response-saturation effects (Figures 7C(ii) and 7D). This "inverted coupling," combined with the metabolic demand of the seizure activity, appears to drive a marked decrease in HbO and increase in HbR, suggesting significant hypoxia within the tumor region during seizure activity.

These trends in both the tumor and non-tumor regions were recapitulated in both of the other seizure events recorded (Figure S9; Video S5). These results suggest that the combination of glioma-induced seizures and region-specific disruptions in neurovascular coupling results in significant hypoperfusion and hypoxia of the tumor tissue during seizure events.

DISCUSSION

This study used WFOM of both GCaMP6f and hemodynamics in awake mice at multiple time points during the progression of a diffusely infiltrating glioma. Our analysis revealed a wide range of changes in both neuronal activity and hemodynamics in the cortex that were associated with tumor progression, including disruptions in the synchrony of both neuronal and hemodynamic activity across the brain, alterations in the coupling between stimulus-evoked neuronal activity and blood flow, progressive increases in tumor-associated IIEs, and eventually spontaneous seizures. These results demonstrate the power of WFOM, in combination with modern transgenic fluorescent labeling techniques, to provide new insights into the functional progression of brain diseases *in vivo.* As a platform, WFOM could be used in other models of neurological disease to assess the interplay between cortical activity and disease progression. The method could also be used to evaluate the effects of new therapies for tumor suppression as well as anti-seizure measures on glioma progression and on neuronal activity, neurovascular coupling, and behavior. The multimodal neural and hemodynamic readouts of WFOM provide a further opportunity to interpret and

predict hemodynamic signatures or other functional biomarkers that might be detectable in humans using fMRI.

Glioma Progression Leads to Decorrelation of Neuronal Activity, IIEs, and Seizures

The changes in excitatory neural activity visualized during glioma progression began with attenuation of detectable neural activity that corresponded to a decrease in the density of neurons expressing GCaMP6f within the tumor. There was also a progressive desynchronization of neuronal activity in contralateral brain regions. The cause of desynchronization between the tumor and contralateral cortex could correspond to local changes in neuronal events occurring within the tumor, perhaps, due to alterations in the inhibitory/excitatory balance, but could also represent a disruption of connectivity between cortical regions (Bosma et al., 2008).

Tumor progression was accompanied by the onset of IIEs, which were captured by WFOM as events with characteristic temporal profiles of GCaMP fluorescence and hemodynamics, but which varied substantially in terms of apparent site of initiation, spatial spread, and repetition frequency. Despite the lack of overt behavioral manifestations associated with IIEs, their increasing frequency during glioma progression suggests that IIEs may be more common in tumor patients than previously appreciated. Interictal epileptiform events have long been known to be highly specific, subclinical markers of epilepsy. While the frequency and temporal patterns of interictal discharges do not correlate well with seizure emergence in focal epilepsy syndromes in general, our data here suggest that an increasing frequency of interictal discharges may correlate with, and perhaps even contribute to, the progressive neurological decline seen in glioma patients. Further studies of the potential clinical utility of interictal discharges as a biomarker of tumor progression may be warranted, as well as laboratory investigations into potential interventions aimed at reducing IIE burden.

Three complete, spontaneous generalized seizures were also captured during *in vivo* imaging, occurring at 34 and 35 DPI in two different mice. While the small size of our cohort limited our ability to assess seizure frequency, the fact that these spontaneous events were seen during relatively short imaging sessions suggests that many more could be occurring during the late stages of disease. Notably, all of the generalized seizures that were seen during WFOM were immediately preceded by bursts of high amplitude discharges that appeared to begin at the infiltrative margin of the tumor, and then spread to surrounding cortex. This finding is consistent with electrophysiological data from *ex vivo* slice culture studies as well as clinical observations, suggesting that glioma-induced seizures arise from the infiltrated peritumoral cortex (Pallud et al., 2014; Senner et al., 2004). Our observations of prominent seizure activity in tumor margins, but decreased neuronal activity in the highly cellular core of the tumor, are also consistent with a recent study using intraoperative electrocorticography that showed elevated neuronal hyperexcitability in the infiltrating glioma margin, but not the tumor core (Venkatesh et al., 2019). These comparisons demonstrate the potential for mouse models to recapitulate key patterns of functional alterations seen in glioma patients. Notably, gliomas that harbor isocitrate dehydrogenase (IDH) mutations show a significantly higher frequency of seizures compared to IDH wild-type gliomas (Chen et al., 2017). Analysis of the functional alterations at the infiltrative

margins of IDH mutant gliomas could thus provide new insights into the mechanisms of glioma-induced seizures.

Together, these observations reveal a heterogeneous landscape of functional changes and interactions that occur during glioma progression, including widespread alterations in cortical neural activity leading to interictal discharges, and more severe focal alterations in and around the tumor that may predispose the brain to seizure activity. Marked histopathological findings at the tumor and tumor-margins included infiltration of glioma cells, neuronal loss, reactive gliosis, and vascular changes. These findings implicate the glioma margin as an important place for continued functional characterization to understand the molecular and cellular basis for its role in initiation of epileptogenic activity.

Progressive Disruption of Neurovascular Coupling

Analysis of neural and hemodynamic WFOM data provided clear evidence of glioma-related disruption of neurovascular coupling within tumor-burdened regions of the cortex. The mechanistic basis of normal neurovascular coupling remains poorly defined, but can include contributions from different types of neurons, astrocytes, smooth muscle cells, pericytes, and endothelial cells (Hillman, 2014), all of which may be disrupted by infiltrating glioma cells, as demonstrated by histological analyses (Farin et al., 2006; Watkins et al., 2014). Although our study did not isolate the cellular cause of the neurovascular disruption observed, it is important to note that coupling changes were localized to tumor-burdened cortex, and were observed for a wide range of different neural events, from stimulus-evoked functional responses to IIEs and seizures.

Analysis of cortical responses to tactile whisker stimulation demonstrated that relatively normal-appearing neural and hemodynamic responses are evoked in uninvolved regions of cortex, even at late stages of tumor progression. However, neurovascular responses in glioma-infiltrated regions of the cortex were clearly attenuated. Such focal changes in coupling of hemodynamics to neural activity could impact the reliability of pre-surgical fMRI measurements used to map functional regions proximal to the tumor boundaries (Sakatani et al., 2003; Zacà et al., 2014), but could also potentially serve as biomarkers for disease progression if fMRI analysis is implemented to assess regional alterations in the HRF.

In regard to resting-state fMRI, our results suggest that both neuronal desynchronization and neurovascular disruption could contribute to apparent changes in fMRI-based measures of "functional connectivity" related to tumor progression (Dierker et al., 2017; Hadjiabadi et al., 2018). Nevertheless, these results do suggest a firm physiological basis for studies that have noted the ability of resting state fMRI data to delineate glioma tumor boundaries (Agarwal et al., 2016; Bowden et al., 2018; Chow et al., 2016).

Analysis of neurovascular coupling to IIEs in cortical regions outside the tumor revealed strong positive coupling (functional hyperemia), while the hemodynamic response was attenuated, delayed, and distorted with an initial decrease in HbT in tumor-burdened regions. Our ability to examine these interactions *in vivo*, from the onset of IIEs onward, suggests that this imaging platform could be used to identify methods for reducing IIEs, or

understanding their innate effects on behavior, cognition, and neural dysfunction in the context of glioma progression.

Our observations of neurovascular dynamics during spontaneous generalized seizures also revealed marked differences in neurovascular coupling between tumor-bearing and non-tumor-bearing cortex. Even in non-tumor-bearing cortex with relatively normal coupling, our observations suggest that the hemodynamic response rapidly saturates at a maximal level, while the amplitudes of neuronal activity greatly exceeded normal levels (>100% change in fluorescence) for sustained periods of over 30 s. This condition is likely to result in transient seizure-evoked hypoxia, consistent with studies exploring pharmacologically induced seizures (Ma et al., 2013; Zhao et al., 2009). These brain-wide effects of glioma-induced seizure activity could be a major contributor to the increased morbidity and cognitive decline seen in low-grade glioma patients with intractable seizures (Klein et al., 2003; Rudà et al., 2010).

Within the tumor, altered neurovascular coupling had the exacerbating effect of actively decreasing perfusion of the region during seizure activity. This prolonged hypoperfusion, combined with the marked increase in neuronal activity and associated increase in metabolic demands, should result in severe tissue hypoxia within the tumor-bearing cortex. This observation is important because seizure-evoked hypoxia could provide a mechanistic basis for the effects of seizure activity on tumor progression. Specifically, hypoxia leads to the stabilization and activation of transcription factor HIF1α, which drives the expression of cytokines and growth factors (such as vascular endothelial growth factor) that stimulate microvascular proliferation (Hardee and Zagzag, 2012; Kaur et al., 2005; Monteiro et al., 2017). The resulting abnormal vasculature, which is a histopathological hallmark of glioma progression, can lead to further disruption in vascular perfusion and neurovascular coupling within the tumor. Hypoxia-induced growth factors can also stimulate glioma cell migration and invasion into the surrounding brain tissue (Monteiro et al., 2017). Our results thus suggest that episodes of seizure-induced hypoxia could feed into a vicious cycle of disease progression that includes glioma dispersion and expanding regions of neuronal dysfunction and vascular dysregulation with increasing frequency of seizures that cause progressively larger regions of tissue hypoxia.

This work demonstrates the complex ways in which glioma infiltration has widespread effects on brain synchrony, neuronal function, and neurovascular coupling, profoundly influencing many aspects of brain physiology and metabolism. Our results provide a dynamic picture of the way in which these functional alterations could shape disease progression, and relate to comorbidities such as seizures, exposing new targets for clinical therapies and interventions. Our results also demonstrated the potential of WFOM *in vivo* optical imaging in mice to improve our understanding of these pathophysiological phenomena, while providing a valuable new platform to discover and evaluate new preventive and protective treatments for the neurological consequences of glioma.

STAR★METHODS

LEAD CONTACT AND MATERIALS AVAILABILITY

Further information and requests for resources and reagents should be directed to the Lead Contact, Peter Canoll (pc561@cumc.columbia.edu). Glioma cells generated in this study are available from the Lead Contact with a completed Material Transfer Agreement.

EXPERIMENTAL MODEL AND SUBJECT DETAILS

Animals—All procedures were reviewed and approved by the Columbia University Institutional Animal Care and Use Committee (IACUC).

Thy1-GCaMP6f mouse littermates (C57BL/6J-Tg(Thy1-GCaMP6f)GP5.17Dkim/J, The Jackson Laboratory Stock No. 025393) (Dana et al., 2014) were weaned at postnatal day 21 and housed together in temperature and humidity controlled facilities with 12-hour light/dark cycles and *ad libitum* water and food. Mice of both sexes were used in this study.

Glioma model—The primary diffusely infiltrating gliomas were generated by injecting PDGFA-IRES-Cre expressing retrovirus into the subcortical white matter of transgenic C57BL/6 mice that harbor floxed p53, stop-flox RPL22[HA], and stop-flox mCherry-luciferase. The resulting retrovirus-induced tumors show the histological features of diffusely infiltrating gliomas (A.M., D. Torres, P.C., unpublished data). The mouse glioma cells were isolated from a retrovirus-induced tumor of a male mouse and expanded in culture as previously described (Sonabend et al., 2013). Diffusely infiltrating gliomas were induced in adult Thy1-GCaMP6f mice via orthotopic transplantation of these mouse glioma cells as detailed below.

METHOD DETAILS

Preparation of Thy1-GCaMP6f mice for WFOM imaging—Adult (~2.5 months old) Thy1-GCaMP6f positive mice were acclimated to human handling and a running wheel. Following acclimation, mice were anesthetized using isoflurane (3%–4% for induction, 2% for maintenance), placed in a stereotaxic frame with ear bars (Kopf) on top of a homeothermic heat pad (temperature maintained at 37°C) and injected with buprenorphine analgesic (0.05 mg/kg). An incision was made and scalp overlying the superficial cortical area excised. The dorsal skull surface was thinned to transparency using a dental drill (Aseptico) with a 0.9 mm stainless steel burr (Fine Science Tools) while irrigating often with sterile 0.9% saline. Immediately after skull thinning a small hole was created using a 20 g needle and glioma cells were injected into the subcortical white matter of right frontal cortex (stereotaxic coordinates relative to bregma = 2.0mm anterior, 2.0mm lateral, 1.5 mm deep) using a Hamilton syringe with a 33 g needle (5×10^4 cells in 1 μL at a flow rate of 0.25 μl/min). For control, sham injected mice, saline was injected into the same coordinates following the same procedure. For the glioma cohort, two female mice (1 and 2) and one male mouse (3) were injected with glioma cells. For the sham-injected cohort, two female mice were injected with saline for histological analysis, and one female and one male mouse were injected with saline and used for widefield optical mapping.

The skull was allowed to dry and liquid cyanoacrylate glue was applied in a thin layer, simultaneously covering the injection hole. The bordering skin was sealed with cyanoacrylate tissue adhesive and gel cyanoacrylate glue was used to bond a custom laser-cut acrylic plastic head plate to the border of the skull. Silicone elastomer was applied to the surface of the skull to further protect the preparation during recovery, and reapplied between imaging sessions. Implanted animals were housed in separate cages and allowed to recover for 72 hours with continued buprenorphine analgesic administration and twice-daily monitoring.

After recovery, in-vivo imaging (details below) was conducted 3–5 times a week for up to 36 days post-injection. During the first week of imaging, animals also underwent 15–30 minute sessions in identical restraint hardware, separate from imaging, to improve acclimation. Animals were monitored daily for symptoms of tumor burden, and in cases where they exhibited signs of terminal morbidity they were euthanized via cardiac perfusion under 5% isoflurane with PBS and brains were extracted and fixed in 10% neutral buffered formalin.

WFOM functional imaging data acquisition—WFOM was conducted to collect simultaneous reflectance and GCaMP6f fluorescence signal as previously described in Ma et al. (2016a), using high-speed strobed LED illumination (band-pass filtered to be centered at 490, 530 and 630 nm) time-locked with an sCMOS camera (Andor Zyla) acquiring at 50.25 Hz. Reflectance and fluorescence emission light from the brain was collected with a 500–640 nm bandpass filter to reject illumination wavelengths and focused using an AF Micro-NIKKOR 60 mm lens (Nikon). Webcam monitoring of the mouse was collected throughout imaging with infrared illumination.

Mice were imaged longitudinally throughout the period of tumor development, starting at 4 days post glioma cell injection, with each mouse having at least 8 imaging sessions. Each animal was head-restrained for a maximum of two hours per imaging session. Resting state recordings involved 12 to 18 recordings (180 s duration each) over the course of each imaging session. For whisker barrel stimulation, recordings were 30 s in duration (10 s pre-stimulation, 5 s whisker stimulation, 15 s post-stimulation). Stimulation was achieved using a small bar attached to a computer-controlled stepper motor positioned to brush the whiskers in an up-down motion at 20 Hz during the stimulus period. A total of 30 recordings were performed for each of the right and left whiskers per imaging session.

Preparation of Thy1-GCaMP6f mice for in-vivo two-photon microscopy—For implantation of cranial windows for two-photon intravital imaging (Figure S2), mice were anesthetized as detailed above and immobilized in a stereotaxic frame. Mice were injected with dexamethasone (1 mg/kg) intramuscularly to prevent brain swelling. The head was shaved, the skin was incised, and the skull was cleared of any residual connective tissue. Two craniotomies were performed, each 4 mm in diameter, using a dental drill over the parietal bones on both hemispheres. Glioma cells were injected into the exposed cortex of the right hemisphere (sterotaxic co-ordinates relative to bregma = −1.5 mm posterior, 2 mm lateral and 1 mm deep), using a Hamilton syringe with a 33 g needle (5×10^4 cells in 1 μL at a flow rate of 0.25 μl/min). The left hemisphere was not injected and served as internal control. Each craniotomy was subsequently sealed with artificial CSF and a 5 mm glass

coverslip using liquid cyanoacrylate glue. A custom laser-cut acrylic plastic head plate was cemented onto the skull using gel cyanoacrylate glue and dental acrylic to allow for head restraint during imaging. Mice were allowed to recover for 72 hours with continued buprenorphine analgesic administration and twice-daily monitoring before two-photon intravital imaging.

Two-photon intravital imaging—Mice were imaged awake and head-restrained in a custom-designed imaging enclosure starting at 4 days post-injection, twice a week for four weeks. Imaging was performed under an upright ThorLabs Bergamo II two-photon microscope running Scanimage, and equipped with a Ti-Sapphire laser (Coherent) and a 16 × /0.8NA water-immersion Nikon objective. GCaMP6f signal was excited using a wavelength of 920 nm. Multiple three-minute runs were acquired in a bidirectional mode with a field of view covering 415 × 415 μm (512 × 512 pixels) and at a frame rate of 30 Hz starting from the brain surface and reaching a depth of 400 μm.

For acute brain slice imaging, the animal was heavily anesthetized and perfused with phosphate buffered saline. The brain was quickly removed and cut coronally into a 2mm thick slice, and immediately imaged using two-photon microscopy to obtain the images shown in Figures S2A and S2B. The remainder of the brain tissue was placed into formalin and processed to produce the images in Figures S2E–S2G.

Histological preparation of brain sections for confocal microscopy—
Histological analysis of free-floating sections was performed on 2 identically-prepared tumor bearing female mice that did not undergo *in vivo* imaging (Figures 1 and S1A), two sham-injected female mice (Figure S4E shows images of one representative mouse), and the formalin-fixed anterior portion of the brain from a mouse that underwent two-photon intravital imaging (Figures S2E–S2G). Coronal sections of 40 μm thickness were obtained on a vibratome. Sections were washed in PBS prior to being delipidated and decolorized in sequential incubations in ½-dH$_2$O diluted CUBIC reagent 1A (10% w/w Triton X-100, 5% w/w Quadrol, 10% w/w Urea, 25 mM NaCl; 30 minutes at room temperature), followed by incubation in complete Reagent 1A for 3.5 hours at 37°C with gentle shaking (Pavlova et al., 2018; Susaki and Ueda, 2016). Following PBS washes, the sections were blocked in PBS containing 10% v/v Normal goat serum and 0.3% w/w Triton X-100. Primary antibody incubations were performed at 4°C for 72 hours followed by secondary antibody incubation for 6 hours at room temperature. Confocal images of CUBIC Reagent 1A clarified coronal brain sections were captured using 488 nm, 561 nm and 639 nm excitation on a Zeiss LSM 800 confocal microscope. Low-power scans of coronal sections were acquired using a 20 × / 0.75 NA objective. High-power images were acquired with a 40 × /1.3 NA oil immersion objective. Maximum projections of Z stacks were generated using FIJI/ImageJ. Multi-region images were field-flatness corrected and stitched using MATLAB™. Secondary-only (no primary antibody) controls confirmed specificity of AQP4 and CD34 antibodies (Figure S1F).

Post mortem histological imaging of whole brain tissue by two-photon microscopy—Whole fixed brains of mice that underwent *in vivo* imaging were clarified using the CUBIC-cancer method as described in Kubota et al. (2017). Briefly, excised brains

were delipidated in ½-dH$_2$0 – diluted CUBIC-L solution (10w%/10w% N-butyldiethanolamine/Triton X-100) for 6 hours followed by incubation in complete CUBIC-L for 5 days with gentle shaking at 37°C. Brains were subsequently washed with PBS and blocked in 10% normal goat serum, 0.5w% Triton X-100 for 6 hours, followed by staining with the indicated primary antibodies (Figures S1C and S1D) for 5 days at room temperature in blocking buffer. After multiple PBS washes, secondary antibody incubations were performed for an additional 4 days at room temperature in blocking buffer. Following final PBS washes, brains were immersed in CUBIC-R solution (45w%/30w% antipyrine/nicotinamide) and stored and imaged in the same solution. High-resolution images of CUBIC-cancer clarified post-mortem brains were acquired using a Nikon A1RMP multiphoton confocal microscope and a 25 × /1.10 NA coverslip-corrected water immersion IR lens objective. For two-photon acquisition, a Chameleon II laser was tuned to 820 nm and images were captured on a spectral detector. Images were taken at 5 μm steps, unmixed and stacks were generated with NIS Elements AR or FIJI/ImageJ software.

QUANTIFICATION AND STATISTICAL ANALYSIS

Conversion of raw WFOM data—Reflectance images from red (630 nm) and green (530 nm) illumination were converted using the modified Beer-Lambert method and available hemoglobin absorption spectra into changes in oxygenated (HbO) and deoxygenated hemoglobin (HbR) concentrations (Ma et al., 2016a). Total hemoglobin (HbT) was calculated as the sum of HbO and HbR. Fluorescence signal (excited at 490 nm) was converted to F/F (mean normalized) and corrected for hemodynamic contamination using the Excitation-Emission ('Ex-Em') method as described in Ma et al. (2016a) which estimates excitation and emission attenuation of the fluorescent light using the simultaneously measured dynamics of HbO and HbR. Excitation and emission pathlength coefficients were estimated according to optimal fluorescence signal correction, and these coefficients were permitted to change during the course of tumor progression due to possible changes in optical properties of the cortex.

After conversion, data for each mouse was registered to the field of view of its first recording session. Epochs where the animal was neither walking nor running were identified using a thresholded standard deviation of adjacent webcam frames and used for subsequent functional connectivity analysis. Data was corrected for minor flickering from illuminating LEDs by division by the mean full image time course and multiplication with the low-pass filtered full image mean time course.

Functional connectivity analysis—K-means clustering (Pearson Correlation distance, k = 22) was applied to the first session of GCaMP6f resting state data in each mouse to identify functional regions of interest based on temporal similarity. Pearson correlation analysis was then applied pixel-by-pixel to both GCaMP6f and HbT data following preconditioning with a 5×5 pixel spatial box filter. Functional regions (glioma injection site, contralateral to glioma, forepaw, whisker barrel and visual cortex) were selected from k-means clusters.

Whisker stimulus response analysis and deconvolution—WFOM data was pre-processed using principal component-based denoising as well as detrending to remove drift, in addition to hemodynamic correction of GCaMP signals as detailed above. Data was then examined to remove trials in which the animal ran or moved significantly within 5 s of stimulus delivery (based on neuronal responses within the hindpaw region). Functional stimulus response maps for GCaMP, HbO, HbR and HbT were generated by averaging remaining trials together, and then averaging the resulting image sequence over the 5 s stimulus duration after subtraction of the average pre-stimulus image.

For time-course extraction, functional regions of interest were identified using k-means clustering of resting state trials as detailed above. Time-courses were then extracted from pre-processed data using the mean average over the ROIs nominally corresponding to motor, forepaw, hindpaw and whisker regions bilaterally (ROIs 1–4 and 5–8 in Figures 3 and S6) for all whisker stimulation trials. Trials not excluded by the criteria above were then averaged to yield region-specific GCaMP, HbO, HbR and HbT whisker stimulus responses, as differences relative to the pre-stimulus mean. Error bars show standard error on the mean across trials. Only responses for delivery of contralateral stimulation are shown, e.g., ROIs 1–4 correspond to right whisker stimulation responses, whereas ROIs 5–8 show responses to left whisker stimulation.

Deconvolution was performed on the average responses for each ROI for each mouse, with GCaMP being deconvolved from each of HbO, HbR and HbT to yield a 'hemodynamic response function' (HRF) for each. Deconvolution was performed using a regularized convolution matrix approach in MATLAB (Ma et al., 2016b). The same regularization was used across all animals and ROIs, optimized using correlation coefficients between the original hemodynamic data and the convolved prediction. In all cases, a 3 s delay was introduced between the GCaMP and hemodynamic traces prior to deconvolution to allow the output to include prediction of pre-neural event dynamics. The units for the deconvolved responses and the summary metric shown in Figures 3D and 3E, correspond to deconvolution of % fluorescence changes from μM hemoglobin concentrations.

Interictal event analysis—Event onset analysis maps shown in Figure 4D were generated by finding the peak time of each IIE from a representative GCaMP time-course. Data in this case was acquired at 25.8 Hz. For each event, a 0.3 s epoch (8 time-points) spanning the peak was examined for every pixel, after down-sampling the image to 64×64 pixels to improve signal to noise. A threshold corresponding to 20% of the maximum GCaMP value across the cortex at the peak time was chosen for each event. For pixels whose maximum within the event epoch exceeded this threshold, we calculated the time taken for the GCaMP6f signal to rise to this threshold value, improving precision by spline interpolating time-courses 10x to 258 Hz. The resulting colormap for each event depicts time taken for each location to reach this GCaMP threshold, with the minimum onset time value within the map subtracted such that the earliest location at t = 0 shows the site of first onset. Plots were generated using the contourf function in MATLAB. This onset time analysis was also repeated using 50% of the peak value of each pixel's signal for each event as the threshold (which normalizes for the amplitude of the event at each location). Onset maps in this case had the same general pattern and sites of localization.

To generate the plot shown in Figure 4E, the total number of IIEs identified per session was normalized by the total duration of resting state recordings acquired in minutes to represent changes in IIE frequency observation over the course of tumor development.

For the analysis shown in Figure 5, spike triggered averaging analysis of hemodynamic signals was applied to interictal events (IIEs) observed in resting state GCaMP6f data. The findpeaks MATLAB function was first applied to GCaMP6f data, with events then user-verified to be IEE-type spikes of at least 2% (but typically closer to 10% or more) F/F amplitude and at least 0.1 s in width/duration. Corresponding HbO, HbR and HbT signals were then time-aligned based on these IEE events and averaged. Peak amplitudes for GCaMP and hemodynamic signals averaged across all IIEs from all sessions for each IIE were calculated by finding the maximum (or in the case of [HBR], the minimum) value and time to half peak, for each mouse as shown in Figures 5C and S8C for each event. Time to half peak was determined by finding the location of the first occurrence of half the previously found peak amplitude in the signal.

To define IIE events as global or local in Figure S7, the findpeaks MATLAB function was used to assess peak prominence and full-width at half-prominence of peaks (Steinmetz et al., 2017). For optimal separation from noise and physiological variations, IIE's were constrained to have a minimum peak of 7%, minimum prominence of 2%, full-width at half-prominence between 0.1 s and 1 s, a prominence to full-width ratio greater than twice the ratio of the total data peak prominences median to total data peak widths median, and at least 10 frames away from the nearest interictal event. Each event was user-verified with time courses and data visualization to eliminate any spurious motion artifact related events. Event image series were thresholded at 6% fluorescence to detect events and observe spatial propagation. IIEs that propagated to involve more than 50% of the masked brain pixels were categorized as global interictal events, whereas those that did not propagate, or involved less than 50% of the cortex were categorized as localized interictal events.

Seizure analysis—Generalized seizure epochs were user-identified and signal time courses were extracted from selected regions of interest within and contralateral to the glioma injection site, as well as from the tumor margin. Predicted HBT signal for a given generalized seizure was estimated using the average HRF of preceding interictal events in the same region of interest as the original signal convolved with the region GCaMP6f time course.

Intravital two-photon image processing and analysis—Two-photon imaging data were motion-corrected by non-rigid transformation using NoRMCorre (Pnevmatikakis and Giovannucci, 2017). Temporal downsampling and spatial binning were applied after motion correction. Principal components analysis (PCA) was used for denoising image data, whereby 50 PCA components were kept for each 3-minute imaging session. We calculated F/F for each pixel using mean intensity as the baseline. ROIs around neuron cell bodies were drawn manually on the maximum intensity projections. Time courses were extracted and analyzed from each drawn ROI using custom MATLAB™ scripts.

Analysis of images from histological sections—Analysis of CD34+ vessels (Figure 1) and GCaMP6f+ neurons (Figure S1) was performed using custom-written macros in FIJI. Briefly, for CD34+ blood vessel analysis, 5 fields from cortical layer 5 of the contralateral hemisphere and tumor-bearing cortex were sampled per mouse. CD34+ area (defined as CD34+ pixels above threshold / total pixels per field) and CD34 fluorescence intensity (defined as average intensity of CD34+ pixels above threshold per field) were expressed as fold change between tumor-bearing cortex over contralateral, non-tumor, cortex. For counting of neurons, 4 independent fields from cortical layer 5 were sampled from the tumor core, tumor margin, and contralateral cortex for each mouse. Total neurons were quantified using immunohistochemical stains for NeuN. A mask was created using NeuN, which was overlaid on the GCaMP6f channel in order to measure the number of GCaMP6f+ neurons and the GCaMP fluorescence signal.

DATA AND CODE AVAILABILITY

Imaging datasets and code will be made available upon request. Please make all requests to the Lead Contact, Peter Canoll (pc561@cumc.columbia.edu), and he will direct the requests to appropriate authors.

ADDITIONAL RESOURCES

There are no additional resources to report.

Supplementary Material

Refer to Web version on PubMed Central for supplementary material.

ACKNOWLEDGMENTS

REFERENCES

Agarwal S, Sair HI, Yahyavi-Firouz-Abadi N, Airan R, and Pillai JJ (2016). Neurovascular uncoupling in resting state fMRI demonstrated in patients with primary brain gliomas. J. Magn. Reson. Imaging 43, 620–626. [PubMed: 26201672]

Avanzini G, Depaulis A, Tassinari A, and de Curtis M (2013). Do seizures and epileptic activity worsen epilepsy and deteriorate cognitive function? Epilepsia 54 (Suppl 8), 14–21.

Bosma I, Douw L, Bartolomei F, Heimans JJ, van Dijk BW, Postma TJ, Stam CJ, Reijneveld JC, and Klein M (2008). Synchronized brain activity and neurocognitive function in patients with low-grade glioma: a magnetoencephalography study. Neuro Oncol. 10, 734–744. [PubMed: 18650489]

Bowden SG, Gill BJA, Englander ZK, Horenstein CI, Zanazzi G, Chang PD, Samanamud J, Lignelli A, Bruce JN, Canoll P, and Grinband J (2018). Local glioma cells are associated with vascular dysregulation. Am. J. Neuroradiol. 39, 507–514. [PubMed: 29371254]

Buckingham SC, Campbell SL, Haas BR, Montana V, Robel S, Ogunrinu T, and Sontheimer H (2011). Glutamate release by primary brain tumors induces epileptic activity. Nat. Med. 17, 1269–1274. [PubMed: 21909104]

Campbell SL, Buckingham SC, and Sontheimer H (2012). Human glioma cells induce hyperexcitability in cortical networks. Epilepsia 53, 1360–1370. [PubMed: 22709330]

Campbell SL, Robel S, Cuddapah VA, Robert S, Buckingham SC, Kahle KT, and Sontheimer H (2015). GABAergic disinhibition and impaired KCC2 cotransporter activity underlie tumor-associated epilepsy. Glia 63, 23–36. [PubMed: 25066727]

Chen H, Judkins J, Thomas C, Wu M, Khoury L, Benjamin CG, Pacione D, Golfinos JG, Kumthekar P, Ghamsari F, et al. (2017). Mutant IDH1 and seizures in patients with glioma. Neurology 88, 1805–1813. [PubMed: 28404805]

Chow DS, Horenstein CI, Canoll P, Lignelli A, Hillman EM, Filippi CG, and Grinband J (2016). Glioblastoma induces vascular dysregulation in non-enhancing peritumoral regions in humans. Am. J. Roentgenol. 206, 1073–1081. [PubMed: 27007449]

Clara CA, Marie SK, de Almeida JR, Wakamatsu A, Oba-Shinjo SM, Uno M, Neville M, and Rosemberg S (2014). Angiogenesis and expression of PDGF-C, VEGF, CD105 and HIF-1α in human glioblastoma. Neuropathology 34, 343–352. [PubMed: 24612214]

Cuddapah VA, Robel S, Watkins S, and Sontheimer H (2014). A neuro-centric perspective on glioma invasion. Nat. Rev. Neurosci. 15, 455–465. [PubMed: 24946761]

Dana H, Chen TW, Hu A, Shields BC, Guo C, Looger LL, Kim DS, and Svoboda K (2014). Thy1-GCaMP6 transgenic mice for neuronal population imaging in vivo. PLoS ONE 9, e108697. [PubMed: 25250714]

de Groot M, Reijneveld JC, Aronica E, and Heimans JJ (2012). Epilepsy in patients with a brain tumour: focal epilepsy requires focused treatment. Brain 135, 1002–1016. [PubMed: 22171351]

Dierker D, Roland JL, Kamran M, Rutlin J, Hacker CD, Marcus DS, Milchenko M, Miller-Thomas MM, Benzinger TL, Snyder AZ, et al. (2017). Resting-state functional magnetic resonance imaging in presurgical functional mapping: sensorimotor localization. Neuroimaging Clin. N. Am 27, 621–633. [PubMed: 28985933]

Farin A, Suzuki SO, Weiker M, Goldman JE, Bruce JN, and Canoll P (2006). Transplanted glioma cells migrate and proliferate on host brain vasculature: a dynamic analysis. Glia 53, 799–808. [PubMed: 16541395]

Faught E, Karakis I, and Drane DL (2018). The impact of interictal discharges on performance. Curr. Neurol. Neurosci. Rep 18, 88. [PubMed: 30298240]

Genetti M, Grouiller F, Vulliemoz S, Spinelli L, Seeck M, Michel CM, and Schaller K (2013). Noninvasive language mapping in patients with epilepsy or brain tumors. Neurosurgery 72, 555–565. [PubMed: 23511822]

Gillespie S, and Monje M (2018). An active role for neurons in glioma progression: making sense of Scherer's structures. Neuro Oncol. 20, 1292–1299. [PubMed: 29788372]

Gleiser C, Wagner A, Fallier-Becker P, Wolburg H, Hirt B, and Mack AF (2016). Aquaporin-4 in astroglial cells in the CNS and supporting cells of sensory organs—a comparative perspective. Int. J. Mol. Sci 17, E1411. [PubMed: 27571065]

Hadjiabadi DH, Pung L, Zhang J, Ward BD, Lim WT, Kalavar M, Thakor NV, Biswal BB, and Pathak AP (2018). Brain tumors disrupt the resting-state connectome. Neuroimage Clin. 18, 279–289. [PubMed: 29876248]

Hardee ME, and Zagzag D (2012). Mechanisms of glioma-associated neovascularization. Am. J. Pathol 181, 1126–1141. [PubMed: 22858156]

Hillman EM (2014). Coupling mechanism and significance of the BOLD signal: a status report. Annu. Rev. Neurosci 37, 161–181. [PubMed: 25032494]

John Lin CC, Yu K, Hatcher A, Huang TW, Lee HK, Carlson J, Weston MC, Chen F, Zhang Y, Zhu W, et al. (2017). Identification of diverse astrocyte populations and their malignant analogs. Nat. Neurosci 20, 396–405. [PubMed: 28166219]

Johung T, and Monje M (2017). Neuronal activity in the glioma microenvironment. Curr. Opin. Neurobiol. 47, 156–161. [PubMed: 29096244]

Kaur B, Khwaja FW, Severson EA, Matheny SL, Brat DJ, and Van Meir EG (2005). Hypoxia and the hypoxia-inducible-factor pathway in glioma growth and angiogenesis. Neuro Oncol. 7, 134–153. [PubMed: 15831232]

Klein M, Engelberts NH, van der Ploeg HM, Kasteleijn-Nolst Trenité DG, Aaronson NK, Taphoorn MJ, Baaijen H, Vandertop WP, Muller M, Postma TJ, and Heimans JJ (2003). Epilepsy in low-grade gliomas: the impact on cognitive function and quality of life. Ann. Neurol 54, 514–520. [PubMed: 14520665]

Kubota SI, Takahashi K, Nishida J, Morishita Y, Ehata S, Tainaka K, Miyazono K, and Ueda HR (2017). Whole-body profiling of cancer metastasis with single-cell resolution. Cell Rep. 20, 236–250. [PubMed: 28683317]

Kwong KK, Belliveau JW, Chesler DA, Goldberg IE, Weisskoff RM, Poncelet BP, Kennedy DN, Hoppel BE, Cohen MS, Turner R, et al. (1992). Dynamic magnetic resonance imaging of human brain activity during primary sensory stimulation. Proc. Natl. Acad. Sci. USA 89, 5675–5679. [PubMed: 1608978]

Liu H, Qiu Gp, Zhuo F, Yu Wh., Sun Sq., Li Fh., and Yang M (2015). Lost polarization of Aquaporin4 and dystroglycan in the core lesion after traumatic brain injury suggests functional divergence in evolution. BioMed Res. Int 2015, 471631. [PubMed: 26583111]

Ma H, Zhao M, and Schwartz TH (2013). Dynamic neurovascular coupling and uncoupling during ictal onset, propagation, and termination revealed by simultaneous in vivo optical imaging of neural activity and local blood volume. Cereb. Cortex 23, 885–899. [PubMed: 22499798]

Ma Y, Shaik MA, Kim SH, Kozberg MG, Thibodeaux DN, Zhao HT, Yu H, and Hillman EM (2016a). Wide-field optical mapping of neural activity and brain haemodynamics: considerations and novel approaches. Philos. Trans. R. Soc. Lond. B Biol. Sci 371, 20150360. [PubMed: 27574312]

Ma Y, Shaik MA, Kozberg MG, Kim SH, Portes JP, Timerman D, and Hillman EMC (2016b). Resting-state hemodynamics are spatiotemporally coupled to synchronized and symmetric neural activity in excitatory neurons. Proc. Natl. Acad. Sci. USA 113, E8463–E8471. [PubMed: 27974609]

Mader S, and Brimberg L (2019). Aquaporin-4 water channel in the brain and its implication for health and disease. Cells 8, E90. [PubMed: 30691235]

Monteiro AR, Hill R, Pilkington GJ, and Madureira PA (2017). The role of hypoxia in glioblastoma invasion. Cells 6, E45. [PubMed: 29165393]

Mou K, Chen M, Mao Q, Wang P, Ni R, Xia X, and Liu Y (2010). AQP-4 in peritumoral edematous tissue is correlated with the degree of glioma and with expression of VEGF and HIF-alpha. J. Neurooncol. 100, 375–383. [PubMed: 20467785]

Nagelhus EA, Mathiisen TM, and Ottersen OP (2004). Aquaporin-4 in the central nervous system: cellular and subcellular distribution and coexpression with KIR4.1. Neuroscience 129, 905–913. [PubMed: 15561407]

Nielsen JS, and McNagny KM (2008). Novel functions of the CD34 family. J. Cell Sci 121, 3683–3692. [PubMed: 18987355]

Nielsen S, Nagelhus EA, Amiry-Moghaddam M, Bourque C, Agre P, and Ottersen OP (1997). Specialized membrane domains for water transport in glial cells: high-resolution immunogold cytochemistry of aquaporin-4 in rat brain. J. Neurosci 17, 171–180. [PubMed: 8987746]

Nigim F, Cavanaugh J, Patel AP, Curry WT Jr., Esaki S, Kasper EM, Chi AS, Louis DN, Martuza RL, Rabkin SD, and Wakimoto H (2015). Targeting hypoxia-inducible factor 1α in a new orthotopic model of glioblastoma recapitulating the hypoxic tumor microenvironment. J. Neuropathol. Exp. Neurol 74, 710–722. [PubMed: 26083570]

Noell S, Wolburg-Buchholz K, Mack AF, Ritz R, Tatagiba M, Beschorner R, Wolburg H, and Fallier-Becker P (2012). Dynamics of expression patterns of AQP4, dystroglycan, agrin and matrix metalloproteinases in human glioblastoma. Cell Tissue Res. 347, 429–441. [PubMed: 22307776]

Pallud J, Le Van Quyen M, Bielle F, Pellegrino C, Varlet P, Cresto N, Baulac M, Duyckaerts C, Kourdougli N, Chazal G, et al. (2014). Cortical GABAergic excitation contributes to epileptic activities around human glioma. Sci. Transl. Med 6, 244ra89.

Pavlova IP, Shipley SC, Lanio M, Hen R, and Denny CA (2018). Optimization of immunolabeling and clearing techniques for indelibly labeled memory traces. Hippocampus 28, 523–535. [PubMed: 29663578]

Petrella JR, Shah LM, Harris KM, Friedman AH, George TM, Sampson JH, Pekala JS, and Voyvodic JT (2006). Preoperative functional MR imaging localization of language and motor areas: effect on therapeutic decision making in patients with potentially resectable brain tumors. Radiology 240, 793–802. [PubMed: 16857981]

Pnevmatikakis EA, and Giovannucci A (2017). NoRMCorre: an online algorithm for piecewise rigid motion correction of calcium imaging data. J. Neurosci. Methods 291, 83–94. [PubMed: 28782629]

Raichle ME, MacLeod AM, Snyder AZ, Powers WJ, Gusnard DA, and Shulman GL (2001). A default mode of brain function. Proc. Natl. Acad. Sci. USA 98, 676–682. [PubMed: 11209064]

Robert SM, Buckingham SC, Campbell SL, Robel S, Holt KT, Ogunrinu-Babarinde T, Warren PP, White DM, Reid MA, Eschbacher JM, et al. (2015). SLC7A11 expression is associated with seizures and predicts poor survival in patients with malignant glioma. Sci. Transl. Med 7, 289ra86.

Rudà R, Trevisan E, and Soffietti R (2010). Epilepsy and brain tumors. Curr. Opin. Oncol 22, 611–620. [PubMed: 20706121]

Sakatani K, Murata Y, Fukaya C, Yamamoto T, and Katayama Y (2003). BOLD functional MRI may overlook activation areas in the damaged brain. Acta Neurochir. Suppl. (Wien) 87, 59–62.

Schwartz TH (2007). Neurovascular coupling and epilepsy: hemodynamic markers for localizing and predicting seizure onset. Epilepsy Curr. 7, 91–94. [PubMed: 17694162]

Selvitelli MF, Walker LM, Schomer DL, and Chang BS (2010). The relationship of interictal epileptiform discharges to clinical epilepsy severity: a study of routine electroencephalograms and review of the literature. J. Clin. Neurophysiol 27, 87–92. [PubMed: 20234317]

Senner V, Köhling R, Püttmann-Cyrus S, Straub H, Paulus W, and Speckmann EJ (2004). A new neurophysiological/neuropathological ex vivo model localizes the origin of glioma-associated epileptogenesis in the invasion area. Acta Neuropathol. 107, 1–7. [PubMed: 13680280]

Smith AJ, and Verkman AS (2015). Superresolution imaging of Aquaporin-4 cluster size in antibody-stained paraffin brain sections. Biophys. J 109, 2511–2522. [PubMed: 26682810]

Smits A, and Duffau H (2011). Seizures and the natural history of World Health Organization Grade II gliomas: a review. Neurosurgery 68, 1326–1333. [PubMed: 21307795]

Sonabend AM, Yun J, Lei L, Leung R, Soderquist C, Crisman C, Gill BJ, Carminucci A, Sisti J, Castelli M, et al. (2013). Murine cell line model of proneural glioma for evaluation of anti-tumor therapies. J. Neurooncol 112, 375–382. [PubMed: 23504257]

Steinmetz NA, Buetfering C, Lecoq J, Lee CR, Peters AJ, Jacobs EAK, Coen P, Ollerenshaw DR, Valley MT, de Vries SEJ, et al. (2017). Aberrant cortical activity in multiple GCaMP6-expressing transgenic mouse lines. eNeuro 4, ENEURO.0207–17.2017.

Susaki EA, and Ueda HR (2016). Whole-body and whole-organ clearing and imaging techniques with single-cell resolution: toward organism-level systems biology in mammals. Cell Chem. Biol 23, 137–157. [PubMed: 26933741]

Tewari BP, Chaunsali L, Campbell SL, Patel DC, Goode AE, and Sontheimer H (2018). Perineuronal nets decrease membrane capacitance of peritumoral fast spiking interneurons in a model of epilepsy. Nat. Commun 9, 4724. [PubMed: 30413686]

Torres D, and Canoll P (2019). Alterations in the brain microenvironment in diffusely infiltrating low-grade glioma. Neurosurg. Clin. N. Am 30, 27–34. [PubMed: 30470402]

van Breemen MS, Wilms EB, and Vecht CJ (2007). Epilepsy in patients with brain tumours: epidemiology, mechanisms, and management. Lancet Neurol. 6, 421–430. [PubMed: 17434097]

Vecht CJ, Kerkhof M, and Duran-Pena A (2014). Seizure prognosis in brain tumors: new insights and evidence-based management. Oncologist 19, 751–759. [PubMed: 24899645]

Venkataramani V, Tanev DI, Strahle C, Studier-Fischer A, Fankhauser L, Kessler T, Körber C, Kardorff M, Ratliff M, Xie R, et al. (2019). Glutamatergic synaptic input to glioma cells drives brain tumour progression. Nature 573, 532–538. [PubMed: 31534219]

Venkatesh HS, Johung TB, Caretti V, Noll A, Tang Y, Nagaraja S, Gibson EM, Mount CW, Polepalli J, Mitra SS, et al. (2015). Neuronal activity promotes glioma growth through neuroligin-3 secretion. Cell 161, 803–816. [PubMed: 25913192]

Venkatesh HS, Tam LT, Woo PJ, Lennon J, Nagaraja S, Gillespie SM, Ni J, Duveau DY, Morris PJ, Zhao JJ, et al. (2017). Targeting neuronal activity-regulated neuroligin-3 dependency in high-grade glioma. Nature 549, 533–537. [PubMed: 28959975]

Venkatesh HS, Morishita W, Geraghty AC, Silverbush D, Gillespie SM, Arzt M, Tam LT, Espenel C, Ponnuswami A, Ni L, et al. (2019). Electrical and synaptic integration of glioma into neural circuits. Nature 573, 539–545. [PubMed: 31534222]

Wanner IB, Anderson MA, Song B, Levine J, Fernandez A, Gray-Thompson Z, Ao Y, and Sofroniew MV (2013). Glial scar borders are formed by newly proliferated, elongated astrocytes that interact to corral inflammatory and fibrotic cells via STAT3-dependent mechanisms after spinal cord injury. J. Neurosci 33, 12870–12886. [PubMed: 23904622]

Watkins S, Robel S, Kimbrough IF, Robert SM, Ellis-Davies G, and Sontheimer H (2014). Disruption of astrocyte-vascular coupling and the blood-brain barrier by invading glioma cells. Nat. Commun 5, 4196. [PubMed: 24943270]

Zacà D, Jovicich J, Nadar SR, Voyvodic JT, and Pillai JJ (2014). Cerebrovascular reactivity mapping in patients with low grade gliomas undergoing presurgical sensorimotor mapping with BOLD fMRI. J. Magn. Reson. Imaging 40, 383–390. [PubMed: 24338845]

Zhao M, Ma H, Suh M, and Schwartz TH (2009). Spatiotemporal dynamics of perfusion and oximetry during ictal discharges in the rat neocortex. J. Neurosci 29, 2814–2823. [PubMed: 19261877]

Highlights

- Glioma disrupts neural synchrony between bilateral cortical regions

- Tumor development is accompanied by local changes in neurovascular coupling

- Wide-field GCaMP imaging reveals glioma-induced interictal discharges and seizures
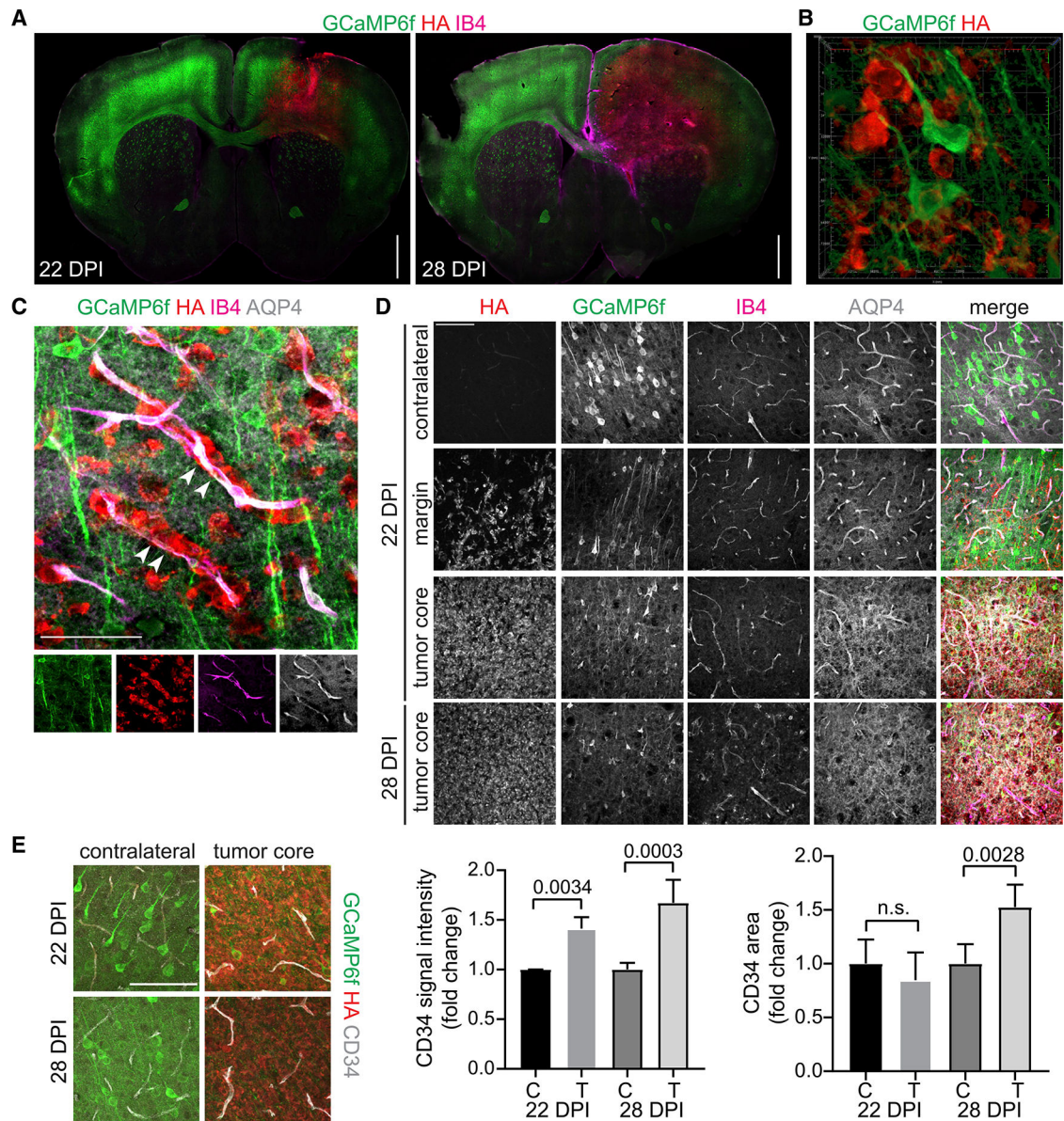
- Altered neurovascular coupling drives hypoperfusion of the tumor during seizures

Figure 1. Immunohistochemical Analysis Reveals Diffuse Infiltration of the Cortex and Progressive Disruption of the Vasculature within the Highly Cellular Core of the Tumor

(A) Coronal sections obtained from glioma-bearing mice at 22 and 28 days post injection (DPI) show the distribution of glioma cells (HA; red), GCaMP6f+ neurons (green), and IB4-labeled vessels (magenta). Stitched images show a single confocal plane. Bar, 1,000 μm.

(B) 3D rendering of GCaMP6f+ neurons (green) surrounded by infiltrating glioma cells (red) (80 × 80 × 15 μm XYZ volume).

(C) Infiltrating glioma cells (red) migrate along blood vessels (arrowheads), with AQP4 (white) remaining closely associated with IB4+ vessels (magenta). Maximum intensity projections of confocal stacks. Bar, 50 μm.

(D) Representative fields of glioma at the indicated time points and locations. AQP4 association with IB4+ vessels is intact in the contralateral (uninfiltrated) cortex and at the infiltrative margins of the tumor, but is disrupted in the tumor core. Bar, 100 μm.

(E) Contralateral cortex and tumor core of a 22- and a 28-DPI tumor stained with CD34. Maximum intensity projections of confocal stack. Bar, 100 μm. Graphs (mean ± standard deviation) show fold change of CD34 signal intensity and area occupied in tumor versus contralateral cortex. C, contralateral cortex; T, tumor core. Two-tailed, unpaired t tests were used to calculate significance.
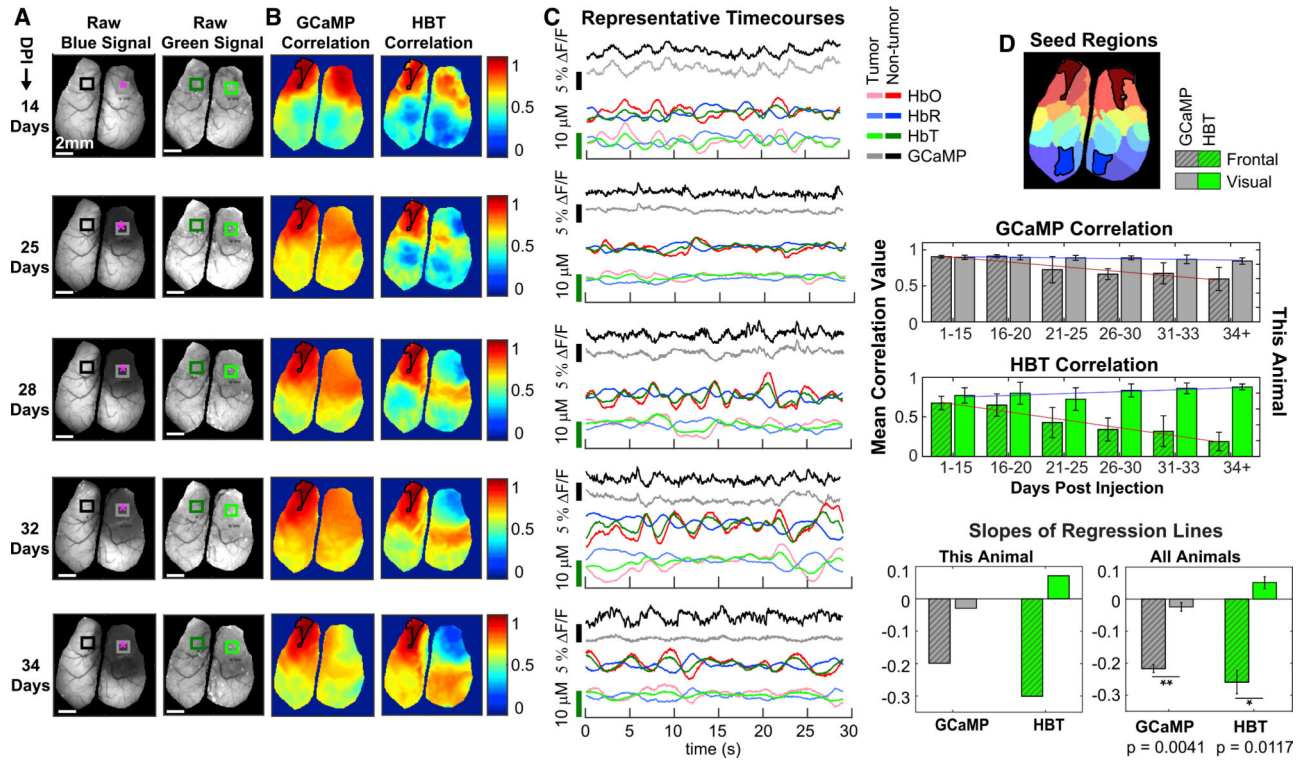
Figure 2. Correlation of GCaMP6f and Hemodynamic Signals between Tumor and Non-Tumor Regions during Tumor Progression (Mouse 2)

(A) Images of raw fluorescence signal showing progressive loss of GCaMP6f fluorescence with no corresponding loss of green reflectance signal. Magenta asterisks indicate glioma injection site. Bar, 2 mm.

(B) Maps of correlation to a seed region, outlined in black, for GCaMP6f and hemodynamic data (HbT).

(C) Time courses taken from representative runs for bilaterally symmetric tumor and non-tumor regions of interest (ROIs) indicated by squares in (A).

(D) Top: k-means clustered regions used to choose frontal cortex (dark red diagonal hatch line fill) and visual cortex (dark blue) regions for correlation analysis. Center: bar plots of both GCaMP6f and hemodynamic correlation between bilateral frontal (gray with diagonal hatch line fill) and visual regions (gray fill) as tumor progresses, shown for one representative animal. Bottom: slopes of regression lines for GCaMP6f and hemodynamic correlation trends for one representative animal, and across all animals (error bars are standard error across animals). Significance across all animals was calculated using paired, two-sample, two-tailed t tests between non-tumor and tumor regions for each channel at significance of *p < 0.05 and **p < 0.005.

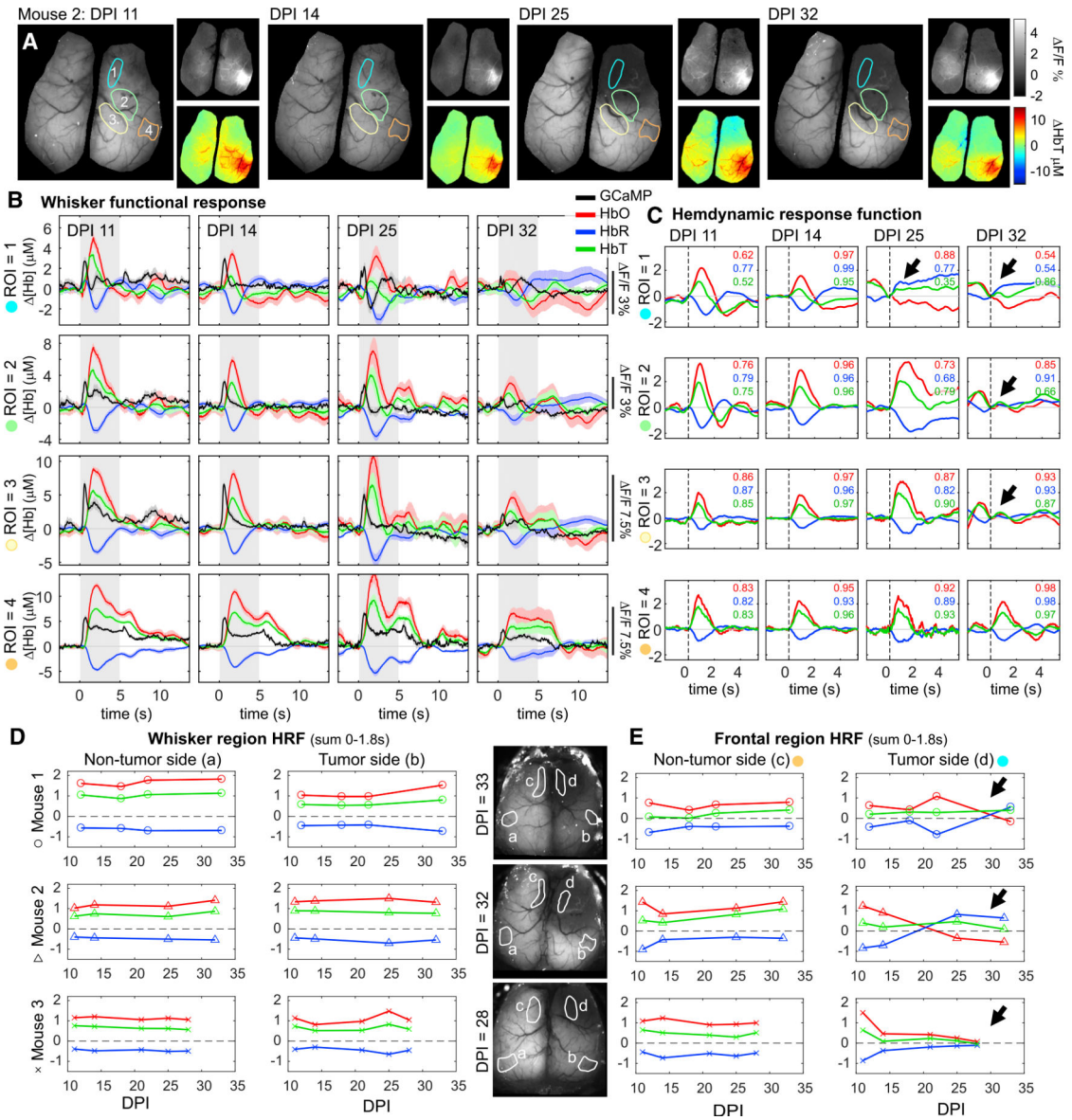Equivalent data for mice 1 and 3 is shown in Figure S3.

Figure 3. Disruption of the Neurovascular Response to Whisker Stimulus during Tumor Progression

(A) ROIs chosen using k-means clustering to correspond approximately to motor, forepaw, hindpaw, and whisker regions (1–4) overlaid on raw GCaMP images from between 11 and 32 DPI (mouse 2). Insets show GCaMP- and HbT-averaged whisker response maps to right tactile whisker stimuli, averaged after exclusion of trials in which the mouse ran (see STAR Methods).

(B) Averaged neural and hemodynamic responses in the ROIs indicated in (A) for each DPI (mouse 2). Note differing amplitude scales for each ROI. Shaded error bounds show SEM.

(C) Hemodynamic response function (HRF) deconvolution results for each ROI and DPI (mouse 2). Here, all plots are shown on the same y axis scale, in most cases demonstrating a consistent relationship between %GCaMP signal change and micron Hb changes, despite the more variable amplitudes of the raw responses in (B). Notable exceptions are seen in

tumor-infiltrated regions, indicated by black arrows. The numbers in color indicate the correlation coefficient between the original data and the HRF convolution fit.

(D) Summary metric calculated as the integral of the first 1.8 s of the HRF (relative to t = 0) across days for each mouse (columns) for ROIs in the unaffected whisker regions (inset image, regions a and c).

(E) Results for frontal ROIs (regions c and d), with "d" corresponding to the tumor in each case. A progressive trend of increasing [HbR] and decreasing [HbO] within the tumor HRF is seen in all mice (arrows).

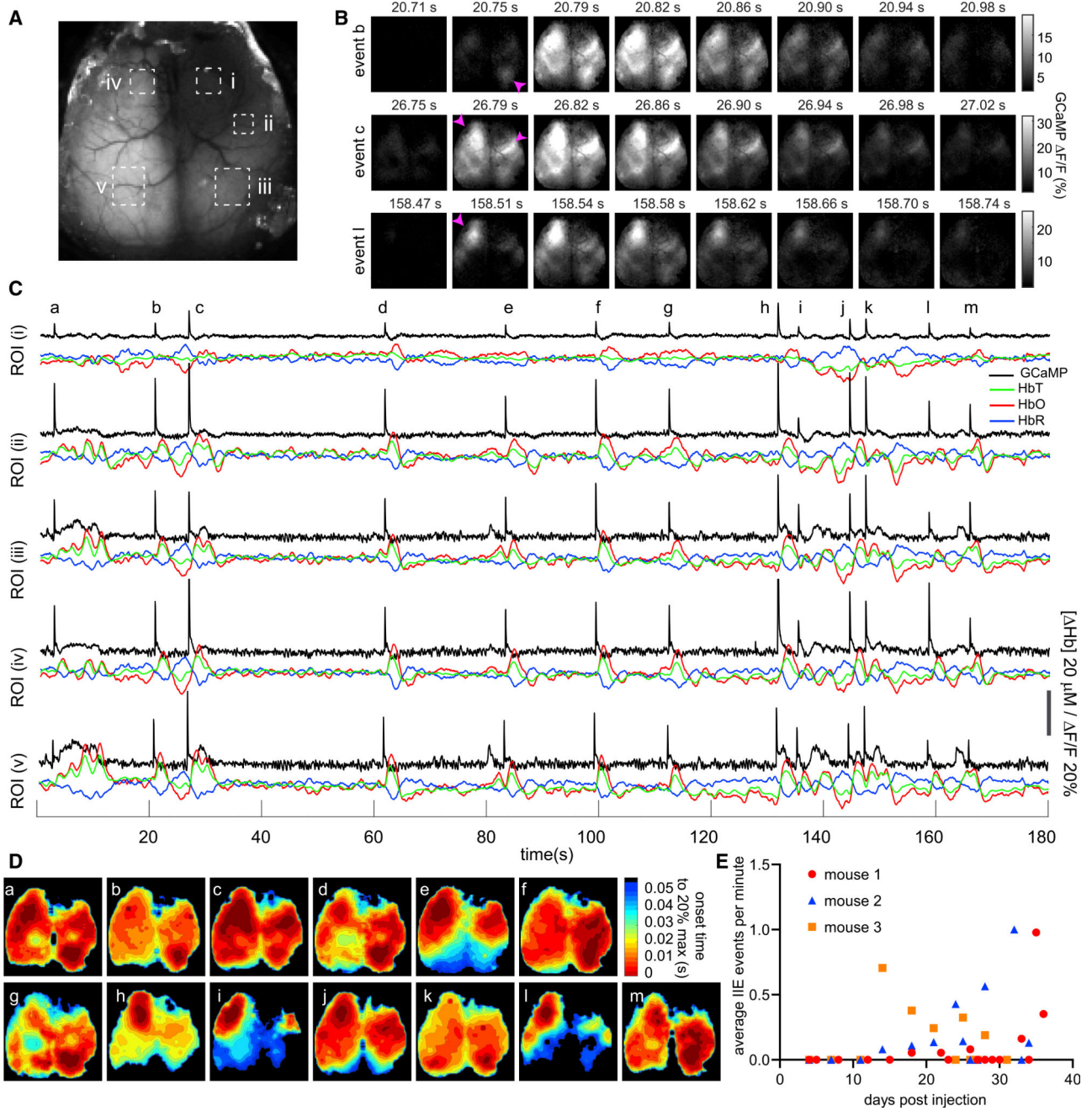See Figures S5 and S6 for further results in mice 1 and 3.

Figure 4. Spatial Variation of Initiation and Propagation of Interictal Events (Mouse 1)

(A) Raw fluorescence image marked with ROIs.

(B)   F/F image time-series of 3 epochs from a 180-s WFOM recording (without external stimulus) containing 13 spatially distinct interictal events (collected at DPI 35). Magenta arrows indicate areas of interictal event initiation.

(C) Time-courses of GCaMP6f fluorescence, HbO, HbR, and HbT extracted from the 5 ROIs in (A). The lower amplitude and altered hemodynamic responses in the tumor region (i) are clearly visible, as well as differing relative amplitudes of the IIEs in each region for each event, reflecting local or global spread.

(D) Contour plots showing the onset time to 20% of the maximum for each of the 13 events (a–m) denoted in (C). Dark red regions correspond to t = 0 initiation locations (see STAR Methods).

(E) Frequency of events for each mouse in each imaging session (all identified events, divided by the total duration of imaging). There is a significant increase in relative frequency of events over time (R = 0.3282, p value = 0.036177).
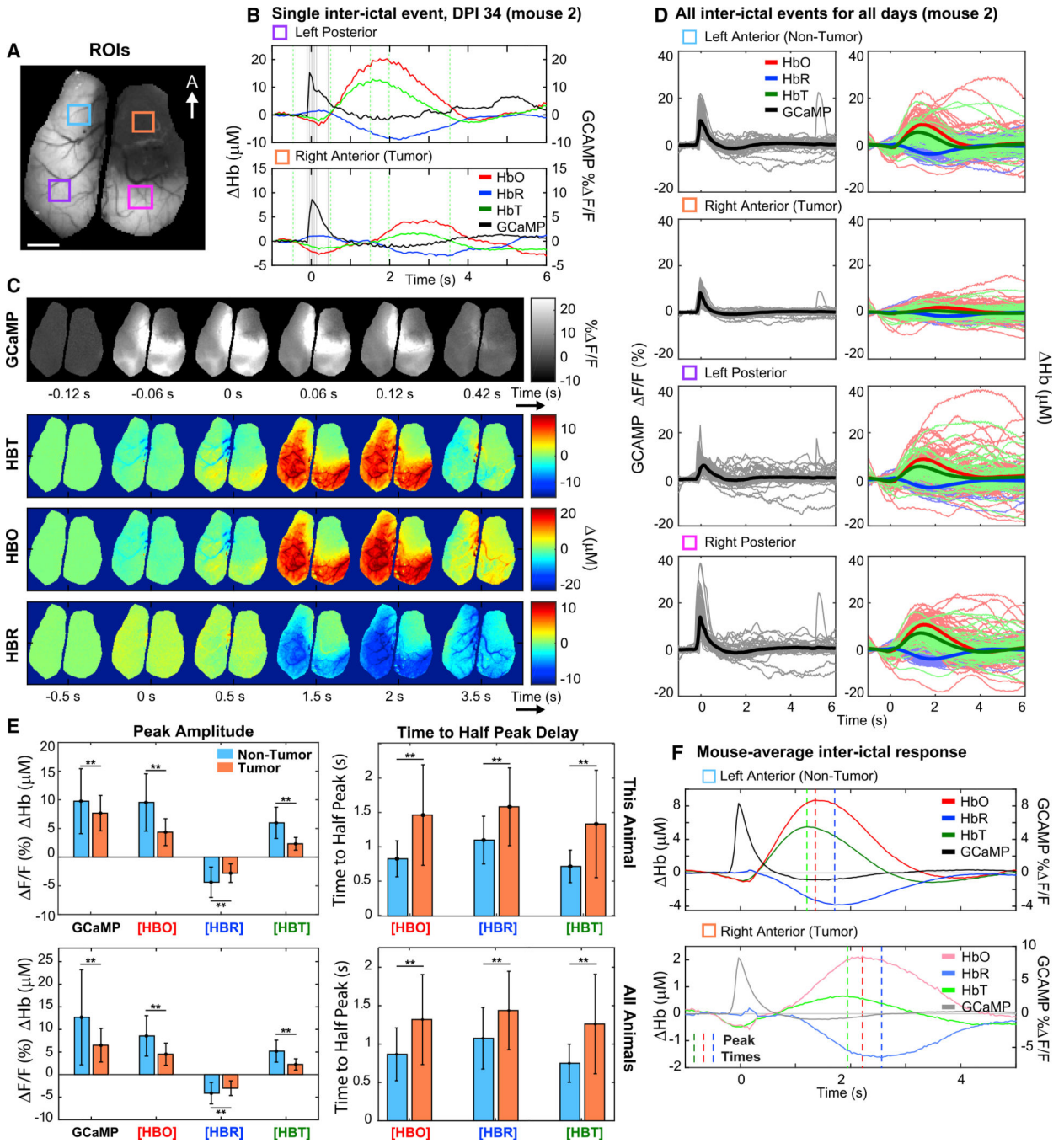
Figure 5. Region-Specific Neurovascular Coupling during Interictal Events (Mouse 2)

(A) Raw fluorescence image marked with ROIs. Bar, 2 mm.

(B) Time series of a single representative interictal event (34 DPI) within in the left posterior and right anterior (tumor) regions.

(C) Image frames corresponding to the event in (B) (timing of frames indicated by gray lines in B for GCaMP6f and dashed green lines for hemodynamics).

(D) Temporally aligned time series for all interictal events across all sessions (all days) in mouse 2; for each ROI in (A), thicker line shows average.

(E) Peak amplitudes of GCaMP6f and hemodynamic responses (left) and time to half-peak of the hemodynamic response (right), for mouse 2 (top row) and across all animals (bottom row). Error bars show standard deviation across trials or across animals, respectively. Significance across all animals was calculated using paired, two-sample, two-tailed t tests between non-tumor and tumor regions for each channel at significance of *p < 0.05 and **p < 0.005.

(F) The overall average response for a non-tumor versus tumor ROI for mouse 2, with vertical bars denoting peak times of each response (note differences in the different Y axes).
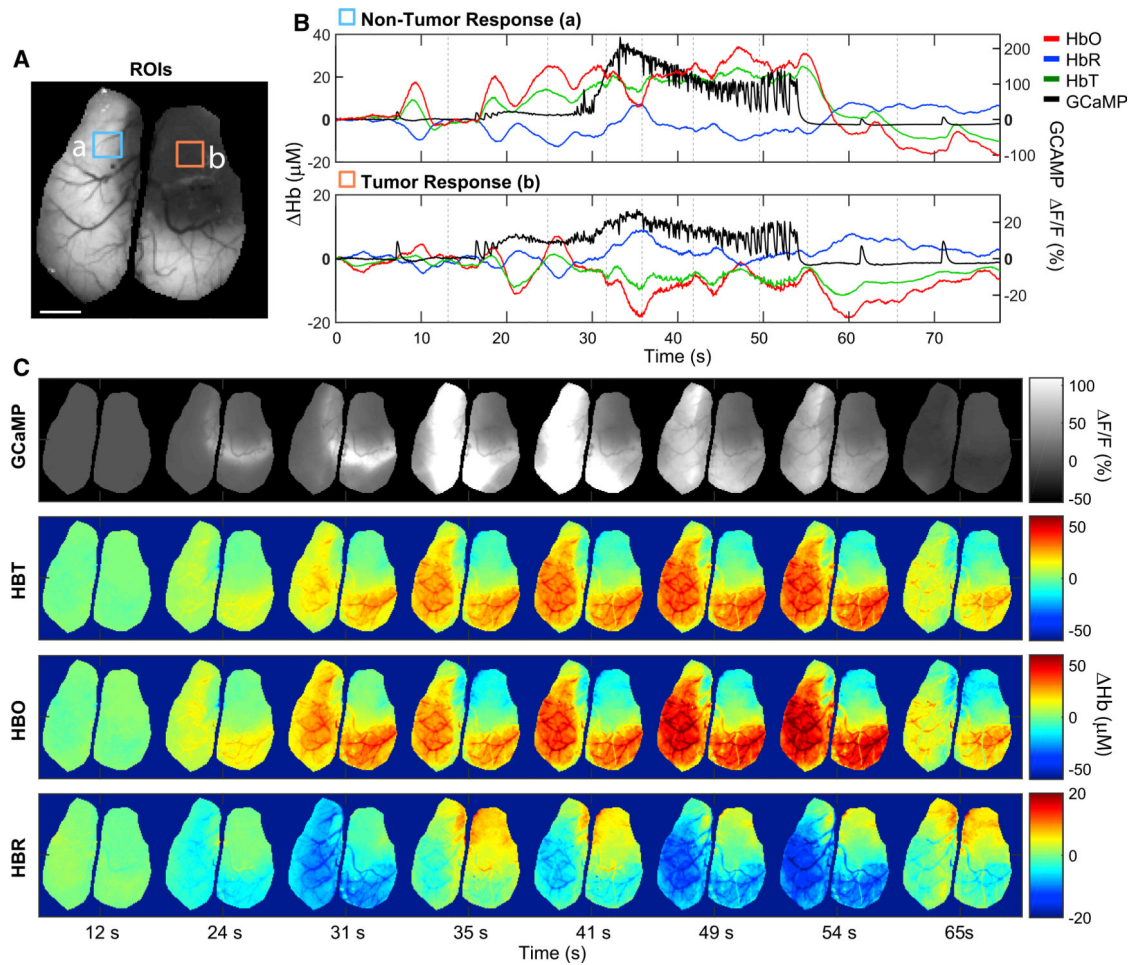
Figure 6. Neuronal and Hemodynamic Activity during a Generalized Seizure (Mouse 2, 34 DPI)
(A) Raw fluorescence image with non-tumor (blue) and tumor (orange) ROIs indicated. Bar, 2 mm.

(B) Time series of a generalized seizure, shown for both GCaMP6f and hemodynamics and averaged across non-tumor and tumor regions.

(C) Spatial patterns of GCaMP6f and hemodynamics shown for frame times indicated by dashed gray lines in (B) during seizure event.
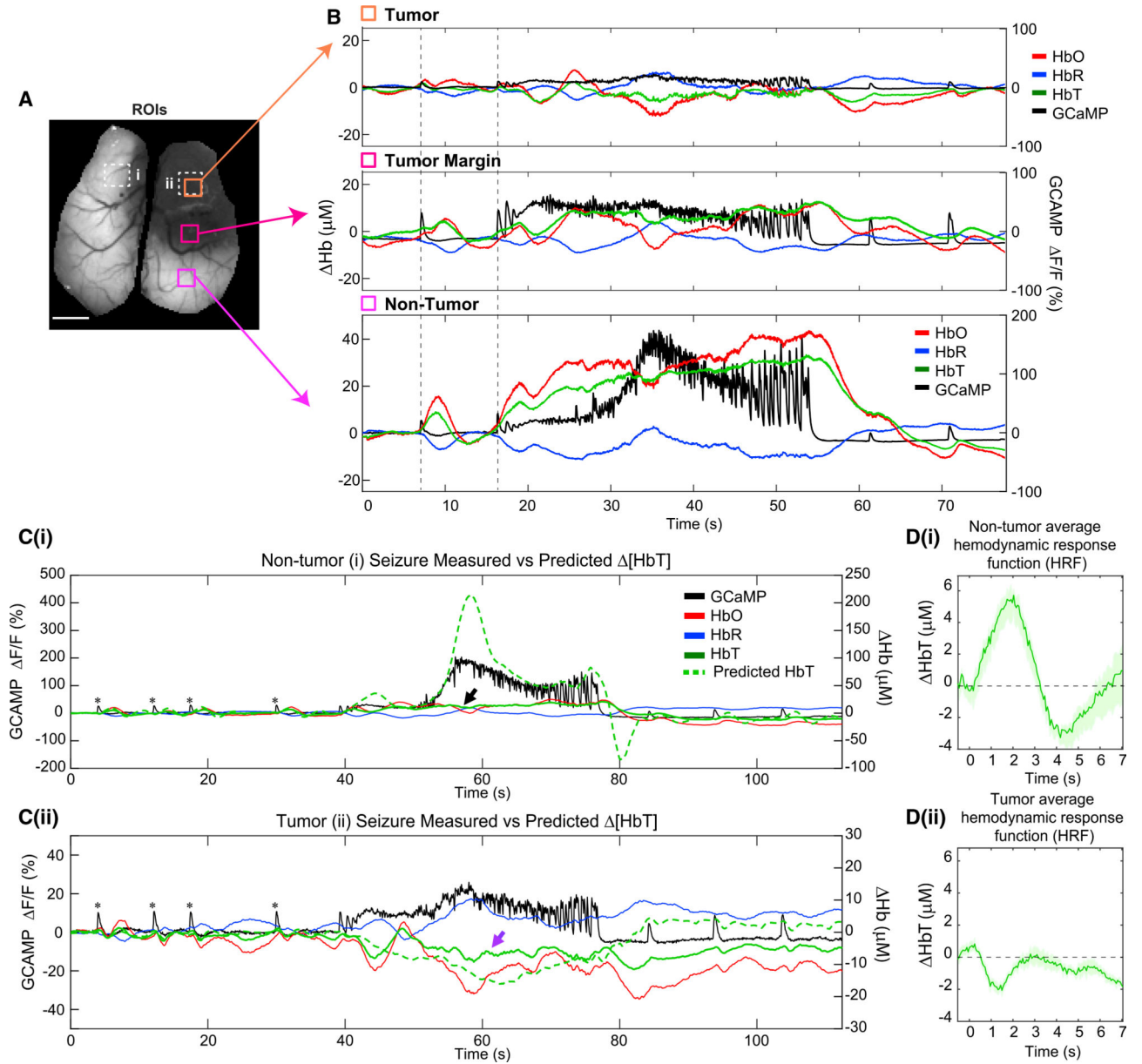
Full seizure shown in Video S4.

Figure 7. Comparing Seizure Activity across the Infiltrative Margin and Model-Based Prediction of the Seizure-Related Hemodynamic Response (Mouse 2)

(A) Raw fluorescence image marked with ROIs. Bar, 2 mm.

(B) Time series of seizure activity for both GCaMP6f and hemodynamics in three regions indicated in (A). Vertical axes are consistent between plots.

(C and D) Time series of seizure activity for both GCaMP6f and hemodynamics for non-tumor (i) and tumor (ii) ROIs indicated in (A). Green dashed lines in (Ci) and (Cii) show predicted change in HbT using convolution of the GCaMP signal with HRFs shown in (Di) and (Dii), derived from the four initial interictal events (indicated with asterisks) for the non-tumor and tumor regions, respectively. Vertical axes are scaled differently to show detail. The measured HbT response in non-tumor regions (black arrow) is significantly lower than predicted by the intense neural seizure activity, suggesting saturation of the hemodynamic

response. In the tumor region, the predicted impaired HbT is similar to the measured HbT response (purple arrow), suggesting that the response seen results from active tumor-evoked constriction of vessels within the tumor.

KEY RESOURCES TABLE

REAGENT or RESOURCE	SOURCE	IDENTIFIER
Antibodies		
rabbit anti-Aquaporin 4	Millipore Sigma	HPA014784; RRID:AB_1844967
rat anti-HA tag	Millipore Sigma	11867423001; RRID:AB_390918
rabbit anti-NeuN	Cell Signaling Technology	12943; RRID:AB_2630395
rabbit anti-CD34	Abcam	ab81289; RRID:AB_1640331
rabbit anti-mCherry	Abcam	ab167453; RRID:AB_2571870
mouse anti-GFAP	Millipore Sigma	MAB360; RRID:AB_11212597
Goat anti-rat Alexa Fluor 568 Conjugate	Life Technologies	A11077; RRID:AB_141874
Goat anti-rabbit Alexa Fluor 633 Conjugate	Life Technologies	A21071; RRID:AB_141419
Goat anti-rabbit Alexa Fluor 568 Conjugate	Life Technologies	A11036; RRID:AB_143011
Goat anti-mouse Alexa Fluor 405 Conjugate	Life Technologies	A31553; RRID:AB_221604
Chemicals, Peptides, and Recombinant Proteins		
Isolectin GS-IB$_4$, biotin-XX Conjugate	Life Technologies	I21414
Streptavidin, Alexa Fluor 633 Conjugate	Life Technologies	S21375
Quadrol	Millipore-Sigma	122262
Urea	Millipore-Sigma	U4883
N-butyldiethanolamine	Millipore-Sigma	L09953
Antipyrine	Fisher Scientific	104971000
Nicotinamide	Fisher Scientific	128271000
Triton X-100	Fisher Scientific	BP151
Deposited Data		
WFOM datasets will be made available on request	This study	N/A
Experimental Models: Cell Lines		
Mouse p53$^{-/-}$ PDGFA+ mCherry-Luciferase$^+$ RPL22^{HA}	This study	N/A
Experimental Models: Organisms/Strains		
C57BL/6J-Tg(Thy1-GCaMP6f)GP5.17Dkim/J	Jackson Laboratory	025393
Software and Algorithms		
FIJI/ImageJ	NIH	https://imagej.net/Fiji
NIS Elements AR v5	Nikon	https://www.microscope.healthcare.nikon.com/products/software/nis-elements/nis-elements-advanced-research
Zen (Blue edition)	Zeiss	https://www.zeiss.com/microscopy/us/products/microscope-software/zen.html
Prism, Version 7	GraphPad	https://www.graphpad.com/scientific-software/prism/
MATLAB 2016a – 2018b	MathWorks	https://www.mathworks.com/products/matlab.html
Modified Beer-Lambert Conversion Excitation-Emission Hemodynamic Correction	Ma et al., 2016a	https://www.ncbi.nlm.nih.gov/pmc/articles/PMC5003860/
Deconvolution Analysis	Ma et al., 2016b	https://www.pnas.org/content/113/52/E8463
Interictal event identification via prominence and full-width at half prominence	Steinmetz et al., 2017	https://www.ncbi.nlm.nih.gov/pmc/articles/PMC5604087/

REAGENT or RESOURCE	SOURCE	IDENTIFIER
NoRMCorre	Pnevmatikakis and Giovannucci, 2017	https://github.com/fiatironinstitute/NoRMCorre